AGU PUBLICATIONS

Water Resources Research

RESEARCH ARTICLE
10.1002/2014WR015490

Key Points:
- A physically based surface resistance model
- Consideration of the dry soil layer thickness when the surface is oven dried
- The hydraulic connection between the soil surface and underneath water source

Correspondence to:
C. Zhang,
chenming.zhang@uq.edu.au

Citation:
Zhang, C., L. Li, and D. Lockington (2015), A physically based surface resistance model for evaporation from bare soils, *Water Resour. Res.*, *51*, 1084–1111, doi:10.1002/2014WR015490.

Received 24 FEB 2014
Accepted 31 DEC 2014
Accepted article online 7 JAN 2015
Published online 23 FEB 2015

A physically based surface resistance model for evaporation from bare soils

Chenming Zhang[1], Ling Li[1,2], and David Lockington[1]

[1]National Centre for Groundwater Research and Training, School of Civil Engineering, University of Queensland, Brisbane, Queensland, Australia, [2]State Key Laboratory of Hydrology-Water Resources and Hydraulic Engineering, Hohai University, Nanjing, China

Abstract The resistance to vapor transfer across the soil-air interface, termed surface resistance, plays an important role in determining the evaporation rate from unsaturated bare soils. A physically based analytical model is developed to describe the surface resistance under varying liquid water saturation. When the vaporization plane remains in the topmost soil layer (TSL), the model considers the vapor transport through the external diffusive layer (EDL), and the hydraulic connection between the capillary water in the TSL and underneath water source for evaporation. When the vaporization plane develops below the TSL, the model predicts the surface resistance by taking into account the development of the dry soil layer, the major barrier for vapor transport at the soil-drying stage. With the consideration of the soil pore size distribution, the model is applicable to different soil types. The model was validated against six sets of laboratory experiments on the drying process of initially water-saturated soil columns under nonisothermal conditions. These experiments were conducted using different soil types and/or heat intensities above the soil surface. The model was found to perform well over intermediate and low liquid water saturation ranges while underestimating the surface resistance for the high liquid water saturation range. The results suggest that the model overall represents reasonably well the processes underlying the vapor transfer across the soil-air interface. Future model improvement may be gained by considering the hydraulic connection between the capillary water and film water in the TSL.

1. Introduction

Evaporation is an important process underlying the mass and heat exchange across the soil-air interface. Understanding the response of evaporation to changes of the liquid water saturation at the evaporating soil surface is important for quantifying the actual evaporation rate. A large amount of research has been directed on the drying process from initially water-saturated bare soils with no external water supply [e.g., *Shimojima et al*., 1990; *Wilson et al*., 1994; *Le Bray and Prat*, 1999; *Yiotis et al*., 2007; *Lehmann et al*., 2008; *Shahraeeni et al*., 2012; *Ren et al.,* 2012]. The drying process can generally be divided into four stages, as shown in Figure 1. During stage I, water is ponded above the soil surface and the evaporation rate decreases over time. Stage II begins when air starts to invade the pore space. At this stage, the near-surface soil layer (a soil layer close to the surface, where the liquid water saturation is measured. It is of a thickness in the centimeter or millimeter range and abbreviated as NSL hereafter) becomes unsaturated, and some dry soil patches start to emerge at the soil surface due to the disruption of hydraulic connectivity to the main water cluster (MWC, defined as water source underneath the soil surface where the liquid water is hydraulically connected, i.e., water-saturated zone and unsaturated zone with liquid water saturation above the residual). In stage III, owing to the significant reduction of wet soil patches and weakening of the hydraulic connection between the soil surface and the MWC underneath, the intensity of the evaporation decreases significantly. Despite the lack of water supply, the vaporization plane where the liquid water is intensively converted into the vapor phase still remains at the soil surface. Further reduction of wet soil patches combined with weakening of the hydraulic connection leads to fast water desaturation of the NSL. The disappearance of wet patches at the soil surface marks the onset of stage IV when the MWC is disconnected from the soil surface (this event is defined as the main cluster disconnection and abbreviated as MCD hereafter) [*Shokri and Or*, 2011]. At this stage, the vaporization plane develops below the soil surface, with a dry soil layer left behind (i.e., above the vaporization plane). Evaporation is sustained by vapor

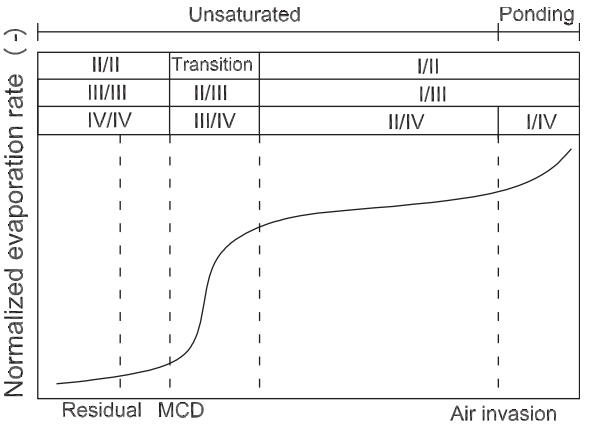

Figure 1. Schematic illustration of the normalized evaporation rate from bare soil without external water supply [e.g., *Le Bray and Prat*, 1999; *Yiotis et al*., 2004]. Four stages are identified: stage I, the initial drying period; stage II, the constant rate period; stage III, the fast falling rate period; and stage IV, the thickening of dry soil layer period. The drying curve is also classified by the two-stage definition [e.g., *Lehmann et al*., 2008; *Shokri and Or*, 2011] and three-stage definition [e.g., *Idso et al*., 1974; *Wilson et al*., 1994; *Rose et al*., 2005; *Smits et al*., 2011] for reference.

generated from the vaporization plane and diffusing through the dry soil layer to the atmosphere. The evaporation rate at stage IV is low and declines further with the thickening of the dry soil layer.

The effect of the liquid water saturation in the NSL on the evaporation rate has been quantified by both empirically and physically based approaches. The empirical approach involves regression analysis on the relationship between surface resistance (typically obtained by inverse calculations from measured evaporation rates) and liquid water saturation. Affected by many other parameters including soil properties (porosity, temperature, and vapor density) and aerodynamic conditions (wind velocity, air humidity, and temperature), a consistent relationship between surface resistance and the liquid water saturation in the NSL could hardly be found. Various analyses have resulted in different functional forms of relationship, including linear [*Camillo and Gurney*, 1986], exponential [*Van de Griend and Owe*, 1994], and power [*Kondo and Saigusa*, 1990; *Daamen and Simmonds*, 1996] functions. Moreover, an obtained function often based on one type of soil does not apply to another soil type [*Smits et al*., 2012].

The physically based approach mainly focuses on the process of vapor movement across an "air layer" from the water-air interface (where vapor is sourced) scattered at the soil surface to a plane-parallel to and above the soil surface. This plane overlaps with an equipotential surface of vapor, i.e., the vapor density on the plane is constant. Although the vapor transport through this layer is driven by both advection and diffusion, the contribution of advection to the evaporative flux is negligibly small compared with the contribution of diffusion [e.g., *Brutsaert*, 1982; *Prat*, 2007; *Shahraeeni et al*., 2012; *Haghighi et al*., 2013; *Or et al*., 2013]. Therefore, this layer is referred to as the external diffusive layer (EDL). The factors that determine the surface resistance are thus the thickness of the EDL and hydraulic properties of the NSL. The thickness of the EDL is related to the atmospheric conditions above the evaporating surface, e.g., higher airflow and evaporative demand in the atmosphere result in thinner EDL [e.g., *Bird et al*., 2002; *Yiotis et al*., 2007; *Shahraeeni et al*., 2012]. The soil hydraulic properties in the NSL, including matric potential, porosity, liquid saturation, and pore size distribution, essentially describe the local water distribution. Despite the complex geometry of the soil matrix, many previous studies conceptualized the NSL as superposition of identical 2-D or 3-D building blocks. The configuration of each building block is supposed to reflect local soil hydraulic properties so that superimposed building blocks are capable of representing the behavior of the soil matrix undergoing the drying process. The vertical configuration of the building block is generally uniform, while the horizontal configurations vary. The extended version of the *Suzuki and Maeda* [1968] model [e.g., *Shahraeeni et al*., 2012; *Haghighi et al*., 2013] conceptualized the top most soil layer (TSL, defined as a layer of soil closest to the free air and of a thickness close to the mean soil particle size) as pinstripes of water-saturated pores and solid planes without vapor flux. Note that the TSL differs from the NSL in scales: the thickness of the TSL depends on soil particle size and hence is in the pore scale; while the thickness of NSL depends on how liquid water saturation close to the soil surface is obtained and is usually in the centimeter or millimeter range. Both the TSL and NSL are illustrated in Figure 2. Under such a configuration, each building block is composed of a stripe of water-saturated pore next to a stripe of solid plane in the transverse cross section, while uniform in the longitudinal cross section. The width of the water-saturated pore stripe corresponds to the effective pore size of the soil, and the width of the solid plane relates to the area of both air-invaded pores and soil grain surface. The area ratio of water-saturated pore to the solid plane equals the volumetric water content in the NSL. To determine surface resistance via the conductance of vapor from NSL to the upper boundary of the EDL, the vapor density is assumed to be saturated at the surface of water-saturated pores

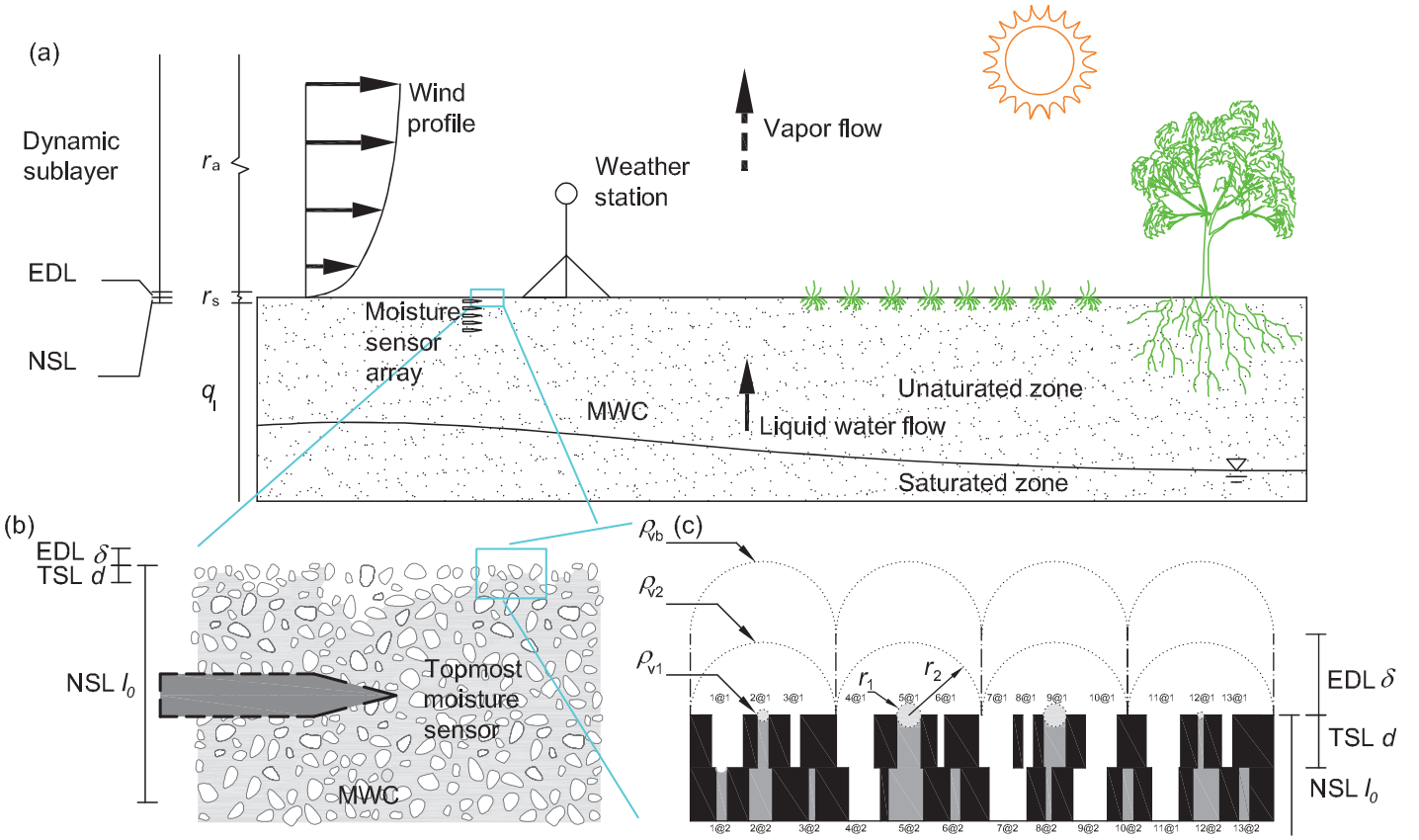

Figure 2. (a) Schematic view of the land-atmosphere interface; (b) cross-section view of the NSL; and (c) cross-section view of the conceptual building blocks representing 3-D EDL and NSL. Four building blocks are displayed with each centered by a water-saturated pores (dark gray). Three equipotential surfaces are specified: equipotential surfaces at the sphere with radius r_1 where vapor density is assumed to be saturated (light gray), equipotential surfaces with radius r_2 that covers the whole surface of the building block, and the equipotential surfaces located at δ above the surface with radius r_2, which are also the upper boundary of the EDL. NSL is conceptualized as a series of slabs after the "cutting and rejoining" treatment (only two layers of NSL are shown in the figure). The TSL is represented by the topmost layer of slab. Under matric potential Ψ_m applied in the NSL, in the TSL, pores 2, 5, 9, and 12 are water-saturated since their radiuses are greater than r_m (the radius corresponding to matric potential Ψ_m by the Young-Laplace equation) and they are connected to the water source underneath; pores 1, 4, 7, and 11 are air invaded because their radiuses are greater than r_m. Although their radiuses are less than r_m, pores 3, 6, 8, and 13 are air invaded due to atmospheric demand for evaporation and lack of water supply from the lower layer. In the layer below the TSL, pores 2, 5, and 12 are still water saturated with radius greater than r_m, as the water-air interfaces of their water bodies are in the TSL with radius less than r_m; pores 4, 7, 9, and 11 are air invaded as the radiuses are greater than r_m and are connected to the atmosphere; water are maintained in pores 1, 3, 6, and 10 owing to their radiuses less than r_m.

and constant at the upper boundary of the EDL, while no vapor flux condition is applied on both the solid plane and the vertical air boundaries of the EDL. Although such a configuration may be able to describe how vapor gets transported through the EDL, it neglects the connectivity of water-saturated pore in the TSL to the MWC underneath, which affects water supply for evaporation. Assuming that both the capillary water and film water are entirely entrapped within the pores by capillary forces, this model overestimates the evaporation associated with the capillary water and does not reflect how film water attached around the soil solid grains by electrical force and van der Waals force contributes to evaporation [*Bear and Cheng*, 2010]. Moreover, this model does not consider the contribution of vapor generated beneath the TSL to evaporation, which plays a major role on maintaining the evaporation rate at stage IV [*Saravanapavan and Salvucci*, 2000; *Shahraeeni et al.*, 2012]. Due to the above mentioned simplifications, this model cannot provide realistic, quantitative predictions surface resistance [*Van Brakel*, 1980; *Shokri et al.*, 2008]. Although the model proposed by *Schlünder* [1988a, 1988b] refined the configuration of the building block as a circular pore located in the middle of rectangular plane, the above mentioned issues remain unaddressed.

On one hand, improving the performance of these physically based resistance models depends on the consideration of the hydraulic connection between the water-saturated pores in the TSL and the MWC at stages II and III. The pore bundle concept has been widely applied to investigate the water permeability in unsaturated soil. This concept assumes that the porous medium is equivalent to stacks of thin slabs. A number of pores parallel with the flow direction were perforated in each slab. The radiuses of the pores follow the

Table 1. Constitutive Relationships Applied in the Model[a]

Parameter	Symbol	Equation	Comment
Vapor diffusivity	D_v ($m^2\ s^{-1}$)	$D_v = 2.29\times10^{-5}\left(\frac{T}{273.15}\right)^{1.75}$	*Saito et al.* [2006]
Saturated vapor density	ρ_v^s)kg m^{-3})	$\rho_v^s = 10^{-3}\exp\left(19.819-\frac{4976}{T}\right)$	*Fujimaki et al.* [2006]
Relative humidity	h_r	$h_r = \exp\left(\frac{\Psi g M_w}{RT}\right)$	Kelvin equation [e.g., *Philip and De Vries*, 1957]
Pore radius	r(m)	$r = -\frac{2\sigma\cos\theta}{\rho_l g\Psi} = \frac{\zeta}{\Psi}$	Young-Laplace equation [e.g., *Lehmann et al.*, 2008]
Tortuosity of vapor	τ	$\tau = \frac{\theta_a^{7/3}}{\theta_s^2}$	*Millington and Quirk* [1961]

[a] T(K) temperature; M_w (0.018 kg mol^{-1}) molecular weight of water; R (8.314 J $mol^{-1}\ K^{-1}$) ideal gas constant; σ (0.072 kg s^{-2}) surface tension; g (9.81 m s^{-2}) magnitude of gravitational acceleration; θ contact angle (0 arc); ζ ($=-2\sigma/\rho_l g$ or -1.469×10^{-5} m^2) a constant assuming θ equals zero.

pore size distribution of the soil. Early researches applied the effective water permeability of one slab to represent the water permeability of the soil [e.g., *Purcell*, 1949; *Burdine et al.*, 1950; *Gates and Lietz*, 1950]. In this representation, water was assumed to only flow through the pores with radiuses less than the pore radius r_m (m) corresponding to the matric potential Ψ_m (m) according to the Young-Laplace equation (Table 1). *Childs and Collis-George* [1950] proposed a series-parallel model to investigate the hydraulic connectivity of two adjacent slabs. This model assumes that the soil behaves the same as perforated slabs, but with the neighboring slab made by "cutting" one perforated slab in two slices and "rejoining" with displacement. As a result, water can only flow through a path made up of two connecting pores from both slabs and with radiuses smaller than r_m. *Mualem* [1976] revised the "cutting and rejoining" concept with the permeability of a path linked to the product of the radiuses of the two connecting pores. A correction function was also adopted in the model to account for the eccentricity and tortuosity between the two joint pores.

On the other hand, further improvement of the physically based surface resistance models lies on the quantification of vapor diffusion through the dry soil layer, which plays a key role at stage IV. Different from the description of past physically based resistance models, no water-saturated pore is present in the TSL during stage IV; instead, the evaporation is maintained by vapor generated from the vaporization plane beneath the dry soil layer. Therefore, to quantify the surface resistance at stage IV requires the description of not only vapor transport from all the pores in TSL (completely dried out) to the upper boundary of the EDL, but also vapor transport through the dry soil layer dominated by diffusion. *Shokri and Or* [2011] observed an immediate jump of the vaporization plane from the TSL to a certain depth below the TSL early in stage IV. They concluded that this jump does not rely on the evaporating intensities but on the bond number (ratio of gravity to capillary force). The depth of the vaporization plane after the jump determines the initial diffusion length of vapor and the highest evaporation rate at stage IV. As the drying process continues, the dry soil layer thickens, resulting in further decrease of the evaporation rate.

In this study, we propose a pore-scale model that describes the surface resistance at the soil-air interface under given matric potential in the NSL. Following the *Schlünder*'s [1988a] method, this model does not specify the water-air interface as a concave surface indented into the soil surface, but a convex surface bulging outward. Also, the model does not specify the upper boundary of EDL as a plane above and parallel to the soil surface. However, the model deals with the hydraulic connection between water-saturated pores in the TSL and the MWC underneath. In addition, the model does not apply a fixed effective pore size to the water-saturated pores, but calculates the surface resistance by integrating the contribution of water-saturated pores of varying sizes following a distribution. Furthermore, the surface resistance after the MCD is obtained with consideration of the dry soil layer development. This model was applied to and validated by the results from six laboratory experiments of evaporation from initially water-saturated soil columns under nonisothermal conditions. The six laboratory experiments distinguish from each other by the soil types and heat intensities applied above the soil surface. A sensitivity analysis was conducted to investigate the responses of surface resistance to the variations of model parameters. This paper is organized as follows: the mathematical considerations of the pore-scale model are introduced in section 2. The experimental setup and procedure of evaporation from 1-D soil column is presented in section 3. The comparison between results from mathematical model and experiments as well as the sensitivity analysis is elaborated in section 4. Discussion of the model assumption is presented in section 5. A summary of findings and conclusions is given in section 6.

2. Theoretical Development

2.1. Evaporation Formulation

Considering the aerodynamic conditions and water availability in the NSL, the evaporation rate from the bare soil surface can be expressed as:

$$E=\frac{\rho_{v1}-\rho_{v\mathrm{Ref}}}{\rho_l(r_s+r_a)}, \tag{1}$$

where ρ_v (kg m^{-3}) is the vapor density; the subscripts *l* and Ref refer to values at the vaporization plane and reference point above the soil surface, respectively; ρ_l (1000 kg m^{-3}) is the density of the liquid water; r_s (s m^{-1}) is the surface resistance; and r_a (s m^{-1}) is the aerodynamic resistance. To facilitate the investigation of the vapor transport regime in the soil-air interface, the vapor density at the upper boundary of the EDL ρ_{vb} (kg m^{-3}) is introduced. Therefore, equation (1) can be rewritten in the form of the following two equations:

$$E=\begin{cases}\dfrac{\rho_{v1}-\rho_{vb}}{\rho_l r_s} & \text{In the EDL,} \quad (2a)\\ \dfrac{\rho_{vb}-\rho_{v\mathrm{Ref}}}{\rho_l r_a} & \text{In the dynamic sublayer.} \quad (2b)\end{cases}$$

The air layers associated with equation (2) are illustrated in Figure 2a. As the vapor transport is dominated by diffusion in the EDL, the surface resistance r_s in equation (2a) can be expressed as follows:

$$r_s=\frac{1}{K_v}=\frac{\delta}{D_v K_{vr}}, \tag{3}$$

where K_v (m s^{-1}) is the vapor conductance through the soil-air interface; D_v (m^2 s^{-1}) is the vapor diffusivity in the air (Table 1); δ (m) is the thickness of the EDL; and K_{vr} $(-)$ is the relative vapor conductance. K_{vr} equals unity when the soil surface is fully covered by liquid water and decreases with the desaturation of the vaporization plane and thickening of the dry soil layer.

For the purpose of convenience, the following subsections focus on the theoretical derivation of K_{vr} rather than r_s. Noting that K_{vr} is jointly contributed to by the vaporization of the capillary water in the TSL at stages II and III, as well as vapor generated from the vaporization plane underneath the dry soil layer at stage IV, we first consider the contribution of each water component to the relative vapor conductance, i.e., K_{vr}^c $(-)$ and K_{vr}^v $(-)$ for capillary water and vapor, respectively. Subsequently, these components are assembled to form an integrated expression of K_{vr}. The evaporation contributed to by the film water is neglected in this study.

2.2. Derivation of K_{vr}^c

The configurations of the NSL and adjacent EDL are depicted in Figure 2c. The soil is comprised of a series of slabs following the "cutting and rejoining" concept [*Childs and Collis-George*, 1950; *Mualem*, 1976]. The TSL is represented by the topmost slab with thickness being equivalent to the average soil particle size *d* (m). The NSL corresponds to the soil layer where the liquid water saturation is measured by the topmost moisture sensor and hence includes a stack of slabs up to a thickness of centimeter scale (Figure 2b). When the matric potential Ψ_m is applied in the NSL, some of the pores in the TSL with radiuses less than r_m are air invaded due to the combined effects of atmospheric demand for evaporation and lack of water supply from pores underneath (e.g., pores 3, 6, 8, and 13 in the TSL). However, in the slab beneath the TSL, some of the pores with radiuses greater than r_m can be water saturated if the water-air interfaces of the water bodies are in the TSL with their radiuses less than r_m. As a result, the effective water content in the TSL $\theta_{le\mathrm{TSL}}$ $(-)$ is less than the effective water content measured in the NSL $\theta_{le\mathrm{NSL}}$ $(-)$. The effective water content θ_{le} $(-)$ describes the volume ratio of the water-saturated pores to the bulk soil under equilibrium.

Under such configuration, one building block is centered by a water-saturated pore with radius r_1, and bounded by a cylinder with radius r_2. The plane surface with radius r_2 covers the area of both soil grains and air-invaded pores (e.g., all the pores with radiuses greater than r_m and air-invaded pores with radius less than r_m). In the TSL, a relationship among r_1, r_2, and $\theta_{le\mathrm{NSL}}$ can be defined as:

$$\frac{\pi r_1^2 d}{\pi r_2^2 d}=\frac{r_1^2}{r_2^2}=\theta_{le\mathrm{TSL}}=G(r_m,r_b,\lambda)\theta_{le\mathrm{NSL}}=G(r_m,r_b,\lambda)\theta_p S_{le\mathrm{NSL}}, \tag{4}$$

where θ_p $(-)$ is the porosity; $S_{le}=\theta_{le}/\theta_p$ $(-)$ is the effective liquid water saturation; and $G(r_m,r_b,\lambda)$ $(-)$ is the correction function to account for the discrepancy between $\theta_{le\mathrm{TSL}}$ and $\theta_{le\mathrm{NSL}}$. Note that this equation is different from the equation proposed by *Suzuki and Maeda* [1968] and *Schlünder* [1988a, 1988b] where the volume ratio of water to the whole building block was set equal to the actual volumetric water content θ_l $(-)$. The modification made is in accordance with the fact that although water filled in the pores is largely in the form of capillary water, film water exists around the surface of the soil grains. Maintained by electrical and van der Waals forces, film water cannot be easily removed unless the local capillary water is dried out and the atmospheric demand for evaporation is strong. The maximum volume of film water determines the residual water content θ_{lr} $(=\theta_p S_{lr}-$, with S_{lr} $(-)$ being the residual liquid water saturation). *Fayer and Simmons* [1995] modified the water retention curve proposed by *Brooks and Corey* [1964] to relate the matric potential to the full liquid water saturation. Their work led to the following expression for S_{le}, which is applicable for describing $S_{le\mathrm{NSL}}$ in equation (4):

$$S_{le}=\frac{S_l-\beta S_{lr}}{1-\beta S_{lr}}=\left(\frac{\Psi_m}{\Psi_b}\right)^{-\lambda}=\left(\frac{r_b}{r_m}\right)^{-\lambda}, \tag{5}$$

where S_l $(-)$ is the actual volumetric liquid water saturation. $\beta=[\ln(-\Psi_0)-\ln(-\Psi_m)]/\ln(-\Psi_0)$ $(-)$ is a parameter for defining a linear relation between S_l below residual and $\ln(-\Psi_m)$. The subscript b and 0 after variables Ψ and r (m) refer to the air-entry values and zero saturation values ($\Psi_0=-5\times10^4$ m), respectively. λ $(-)$ is a parameter related to the pore size distribution.

The correction function G in equation (4) equals 1 when all the pores in the TSL are water saturated (i.e., $r_m > r_b$). With desaturation of the soil, more pores with radiuses less than r_m become air invaded, which results in greater difference between $\theta_{le\mathrm{TSL}}$ and $\theta_{le\mathrm{NSL}}$, or equivalently smaller G. Once the connection between the TSL and the MWC is disrupted during the MCD, the liquid water saturation in the NSL drops below the residual, and no water-saturated pores are present in the TSL, turning G to zero. Following *Mualem* [1976] who uses a power function of effective liquid water saturation to describe the tortuosity and eccentricity between pores in the neighboring slabs, we can express G as:

$$G(r_m,r_b,\lambda)=S_{le}^n, \tag{6}$$

where the exponent n $(-)$ is a fitting parameter. In this study, we aim to obtain a unique value for n that applies to the six experiments examined.

The EDL is located above the soil surface with a thickness of δ. Vapor generated at the water-air interface gets transported by diffusion within the EDL up to its upper boundary where a constant vapor density is maintained. As described by *Schlünder* [1988a, 1988b], the vapor movement from the air-water meniscus to the upper boundary of EDL can be separated into two steps. The first step is featured by vapor diffusing from vapor-saturated equipotential surface to the equipotential surface that encloses the surface of the building block (Figure 2c). The second step is vapor diffusion from the large spherical surface with radius r_2 upward to the upper boundary of the EDL. Assuming that the meniscus of the soil-air interface in the water-saturated pore remains at the upper spherical surface that covers the pore with radius r_1 (Figure 2c), the volumetric vapor flux Q_v^c ($m^3\ s^{-1}$) induced by capillary water in the first step can be expressed by:

$$Q_v^c=\frac{2\pi r_1 r_2 D_v\left(\rho_{v1}^*-\rho_{v2}\right)}{(r_2-r_1)\rho_l}, \tag{7}$$

where the superscript * denotes the saturated vapor density value. According to the Kelvin equation (Table 1), a notable decrease in the relative humidity from unity begins once the matric potential drops below -1×10^2 m. Below this matric potential value, the corresponding liquid water saturation decreases under the residual liquid water saturation for sand and silt, suggesting a downward shift of the vaporization plane to the soil layer below the TSL with a relatively high matric potential and the presence of capillary water. Therefore, it is reasonable to assume that the relative humidity at the vaporization front always equals unity.

Note that this formulation implicitly assumes that the vapor density at the sphere above the meniscus of the water-air interface can be maintained constant (light gray sphere above the meniscus, Figure 2c). In

fact, the vapor density only remains saturated at the water-air menisci as a concave surface indented in the soil surface. Thus, the equipotential surfaces of the vapor density are confocal oblate spheroids in the EDL [*Cooke*, 1967]. However, the locations of the menisci do not significantly affect the relative conductance of vapor. Under the assumption that the surface of saturated vapor density is in a spherical convex shape bulged above the soil surface, the equipotential surfaces in the EDL become confocal spherical surfaces. This can significantly simplify the mathematical formulation for describing vapor transport from water-saturated pores to the top boundary of the EDL. In the second step, the vapor flux from the sphere to the upper boundary of the EDL can be written as:

$$Q_v^c = \frac{\pi r_2^2 D_v(\rho_{v2} - \rho_{vb})}{\delta \rho_l}. \tag{8}$$

Inserting equation (7) to equation (8) to remove ρ_{v2} yields the volumetric vapor flux from the vaporization plane in the TSL to the upper boundary of the EDL in the following form:

$$Q_v^c = \frac{\pi D_v\left(\rho_{v1}^* - \rho_{vb}\right)}{\rho_l\left(\frac{\delta}{r_2^2} + \frac{r_2 - r_1}{2r_2 r_1}\right)}. \tag{9}$$

As a reference, under the same difference of vapor density between the free water surface and the upper boundary of the EDL, the volumetric vapor flux from a building block with water ponded on its surface $Q_{v\mathrm{Ref}}$ ($\mathrm{m^3\ s^{-1}}$) is described by:

$$Q_{v\mathrm{Ref}} = \frac{\pi r_2^2 D_v\left(\rho_{v1}^* - \rho_{vb}\right)}{\delta \rho_l}. \tag{10}$$

Dividing equation (9) by equation (10) yields the relative vapor conductance k_{vr}^c (−) contributed to by a single building block with water-saturated pore radius r_1:

$$k_{vr}^c = \frac{Q_v^c}{Q_{v\mathrm{Ref}}} = \frac{1}{1 + \frac{1}{2\delta}\left(\frac{r_2^2}{r_1} - r_2\right)}. \tag{11}$$

Equation (11) is similar to equation (6) of *Schlünder* [1988b] except that the surrounding solid plane is round in this study rather than being square in the previous work. Inserting equations (4–6) into equation (11) to replace r_2 by r_1, one gets:

$$k_{vr}^c = \frac{1}{1 + \frac{r_1}{2\delta}\left[\frac{1}{\varepsilon}\left(\frac{r_b}{r_m}\right)^{\lambda(1+n)} - \sqrt{\frac{1}{\varepsilon}\left(\frac{r_b}{r_m}\right)^{\lambda(1+n)}}\right]}. \tag{12}$$

Equation (12) only considers the relative conductance of vapor from one building block, of which the water-saturated pore radius equals r_1. To consider the contributions of all the building blocks with different radiuses of water-saturated pores in the TSL, one needs to obtain the expected value of the relative conductance based on the pore size distribution of the soil. The contribution of water-saturated pores of radii in the range between r_1 and $r_1 + dr_1$ to the relative conductance of vapor is given by:

$$dK_{vr}^c = k_{vr}^c f(r_1, r_m) dr_1, \tag{13}$$

where $f(r_1, r_m)$ is the probability density function (PDF) for the water-saturated pores, when the matric potential equal Ψ_m. Based on the water retention curve by *Brooks and Corey* [1964], the PDF and cumulative density function (CDF) of the pore size distribution for the water-saturated pores can be written as:

$$F(r \le r_1, r_m) = \begin{cases} \dfrac{S_{le}(r_1)}{S_{le}(r_m)} = \left(\dfrac{\Psi_m}{\Psi_1}\right)^{\lambda} = \left(\dfrac{r_1 \Psi_m}{\zeta}\right)^{\lambda} & r_1 < r_m \\ 1 & r_1 \ge r_m \end{cases}, \tag{14a}$$

$$f(r_1, r_m) = \begin{cases} \dfrac{\partial}{\partial r_1}\left[\dfrac{S_{le}(r_1)}{S_{le}(r_m)}\right] = \lambda\left(\dfrac{\Psi_m}{\zeta}\right)^{\lambda} r_1^{\lambda - 1} & r_1 < r_m \\ 0 & r_1 \ge r_m \end{cases}, \tag{14b}$$

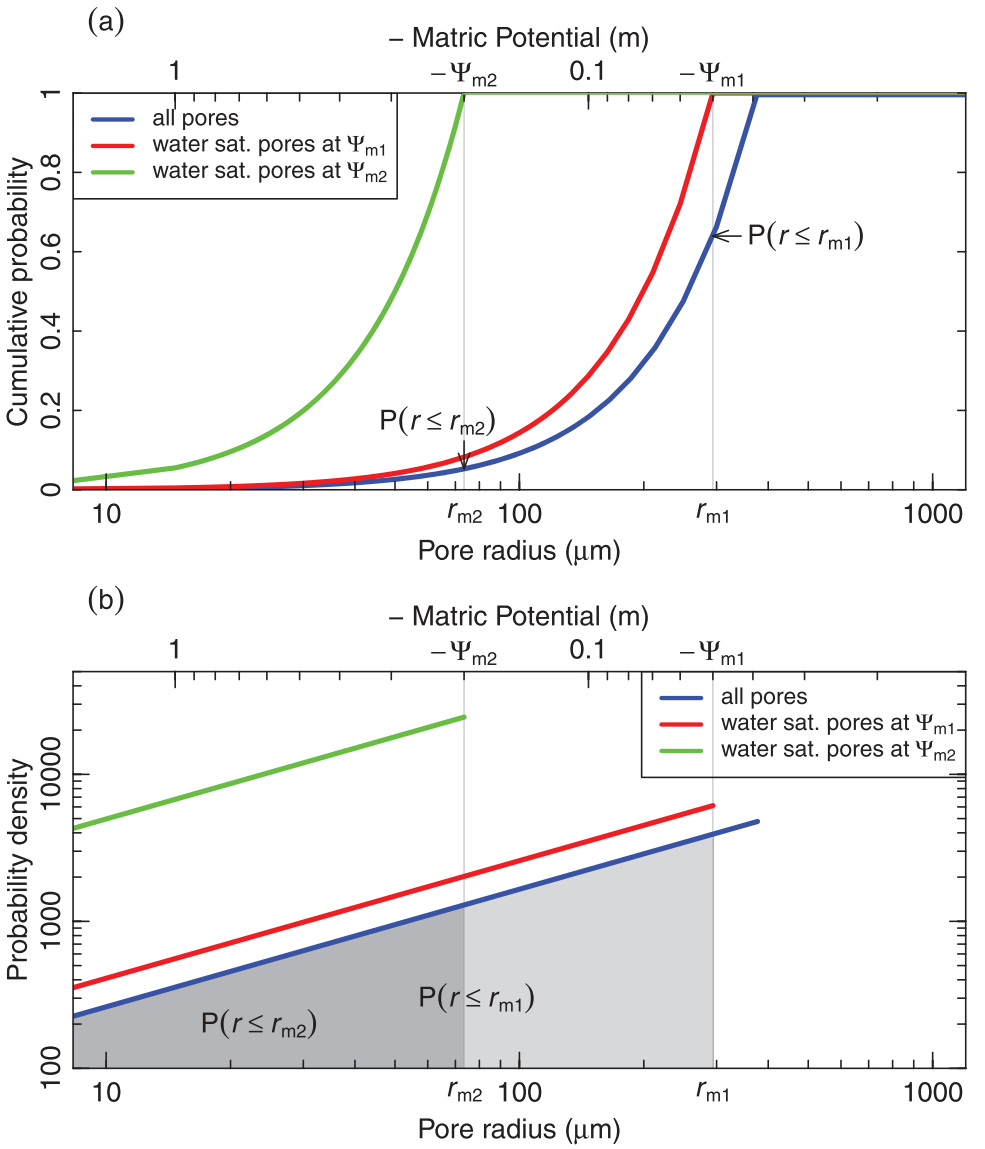

Figure 3. (a) CDF and (b) PDF of water-saturated pore radius at three Ψ_m values (Ψ_b, Ψ_{m1}, and Ψ_{m2}) for medium sand applied in this study. The correlation between pore radius shown on the lower *x*-axis and negative matric potential shown on the upper *x*-axis is established by the Young-Laplace equation. The relation between CDF of all pores (or equivalently, the CDF of water-saturated pores when Ψ_m equals to Ψ_b) and negative matric potential resembles the relation between the effective liquid water saturation and negative matric potential. Therefore, the cumulative probabilities for $r \le r_{m1}$ and $r \le r_{m2}$ equal, respectively, the effective liquid water saturation corresponding to matric potential Ψ_{m1} and Ψ_{m2}. The CDF of water-saturated pores at a given matric potential equals 1 at the potential value. The area shaded in dark gray and total area shaded in dark and light gray (starting from pore radius equal to 0), respectively, represent the cumulative probability of pore radius less than r_{m1} and r_{m2}.

where $F(r \le r_1, r_m)$ is the CDF for the water-saturated pores. Figure 3 shows the CDF and PDF of water-saturated pore radius r_1 when Ψ_m equals to Ψ_b, Ψ_{m1}, and Ψ_{m2}, respectively. When r_m is less than r_b (or equivalently Ψ_m is less than Ψ_b), the PDF and CDF of the water-saturated pores are dependent on r_m (or Ψ_m). The relationship between the CDF and Ψ_m resembling the relationship between S_{le} and Ψ_m described by equation (5). When r_m is greater than or equal to r_b (or equivalently Ψ_m is greater than or equal to Ψ_b), the soil is fully water saturated, and the PDF and CDF of water-saturated pore become independent of r_m.

Inserting equation (14b) into equation (13) and integrate the equation over the water-saturated pore range (from 0 to r_m). One obtains:

$$K_{vr}^{c}=\int_{0}^{r_m}\frac{1}{1+\frac{r_1}{2\delta}\left[\frac{1}{\theta_p}\left(\frac{r_b}{r_m}\right)^{\lambda(1+n)}-\sqrt{\frac{1}{\theta_p}\left(\frac{r_b}{r_m}\right)^{\lambda(1+n)}}\right]}\lambda\left(\frac{\Psi_m}{\zeta}\right)^{\lambda}r_1^{\lambda-1}dr_1$$
$$={}_2F_1\left[1,\lambda;1+\lambda;-\frac{\zeta}{2\delta\Psi_m}\left(\frac{\Psi_m^{\lambda(1+n)}}{\theta_p\Psi_b^{\lambda(1+n)}}-\sqrt{\frac{\Psi_m^{\lambda(1+n)}}{\theta_p\Psi_b^{\lambda(1+n)}}}\right)\right], \tag{15}$$

where ${}_2F_1$ is the hypergeometric function; $\zeta=-2\sigma/\rho_l g$ (m^2) is a constant with σ (0.072 kg s^{-2}) being the surface tension. Equation (15) describes the vapor conductance contributed to by all the water-saturated pores in the TSL, which dominates the evaporation process at stages II and III. A closed-form approximation to equation (15) is provided in the Appendix A.

2.3. Derivation of K_{vr}^{v}

The contribution of the vapor generated at the vaporization plane beneath the dry soil layer to evaporation dominates during stage IV when the dry soil layer emerges. The transport of vapor at this stage comprises three steps: (1) vapor generated at the vaporization plane diffusing through the dry soil layer; (2) vapor from all the pores in the TSL (TSL at this stage is completely dried) expanding to the spheres that cover the surfaces of the building blocks; and (3) vapor from the surfaces of the building blocks diffusing through the EDL. The gradient of the vapor density across the dry soil layer in the first step is significantly higher than those in the other two steps. Assuming that the liquid water saturation in the dry soil layer is zero, one can express the volumetric vapor flux through the dry soil layer to the upper boundary of EDL Q_v^v (kg m^{-3}) as:

$$Q_v^v=\frac{D_v\pi r_2^2\tau_0\theta_p}{\rho_l}\frac{\rho_{v1}^*-\rho_{vb}}{l}, \tag{16}$$

where τ_0 (=0.66–) is the tortuosity when the liquid water saturation is zero; and l (m) is the thickness of the dry soil layer. Determining the volumetric vapor flux through the dry soil layer relies largely on the thickness of the dry soil layer, usually smaller than the thickness of the NSL (e.g., a dry soil layer with thickness at the millimeter scale would have notable influence on the evaporation rate, while the thickness of the NSL is generally at the centimeter scale).

To establish a relationship between the liquid water saturation in the NSL and the thickness of the dry soil layer, we further assume that once the liquid water saturation in the NSL drops below the residual saturation, the NSL is ideally layered by an upper dry soil layer and a lower unsaturated zone of residual liquid water saturation. The liquid water saturation in the NSL is the weighted average of the saturations in both the upper dry soil layer (zero) and the lower unsaturated zone, i.e.,

$$S_{lNSL}=0\frac{l}{l_0}+S_{lr}\frac{l_0-l}{l_0}\Rightarrow l=l_0\left(1-\frac{S_{lNSL}}{S_{lr}}\right)\ \ (\text{when}\ \ S_{lNSL}<S_{lr}), \tag{17}$$

where l_0 (m) is the thickness of the NSL. Equation (17) is only valid when the liquid water saturation in the NSL is below the residual liquid water saturation. If the liquid water saturation in the NSL is above the residual liquid water saturation, evaporation is dominated by the vaporization of the capillary water in the TSL (or equivalently, $l=0$).

According to *Fayer and Simmons* [1995], the component of βS_{lr} in equation (5) is used to describe the relation between matric potential and liquid water saturation below the residual value, which can be conveniently adopted in equation (17). In addition, as found by *Shokri and Or* [2011], the thickening of the dry soil layer during the soil-drying process may not be gradual. The vaporization plane may jump directly from the TSL to a certain depth below the TSL during the MCD. This suggests that once the evaporation proceeds into stage IV, the liquid water saturation in the NSL becomes less than the residual value. With the consideration of the above mentioned factors, we approximate the soil water retention relationship below the residual liquid water saturation based on the model of *Fayer and Simmons* [1995] to express S_{lNSL} in equation (17) as:

$$S_{lNSL} \approx S_{lr} \frac{\ln(-\Psi_0) - \ln(-\Psi_m - \Psi_p)}{\ln(-\Psi_0)}, \tag{18}$$

where Ψ_p (m) is the matric potential corresponding to the initial liquid water saturation at early stage IV. When the matric potential in the NSL is high enough to maintain the hydraulic connection between the TSL and the MWC, S_{lNSL} described by equation (18) remains consistently close to the liquid water saturation corresponding to Ψ_p. This avoids the problem of a negative dry soil layer thickness and singular point (occurs when $S_{lNSL} = S_{lr}$), which would occur if the original soil water retention curve (equation (5)) is used to describe S_{lNSL} in equation (17). Combining equations (16–18) leads to:

$$Q_v^v = \frac{D_v \pi r_2^2 \tau_0 \theta_p}{\rho_l} \frac{\ln(-\Psi_0)(\rho_{v1}^* - \rho_{vb})}{l_0 \ln(-\Psi_m - \Psi_p)}. \tag{19}$$

The ratio of equation (19) to equation (10) yields an expression for the relative conductance of vapor through the soil-air interface contributed to by vapor generated underneath the dry soil layer,

$$K_{vr}^v = \frac{\delta \tau_0 \theta_p \ln(-\Psi_0)}{l_0 \ln(-\Psi_m - \Psi_p)}. \tag{20}$$

Equation (20) physically captures the trend of decreasing vapor conductance (through the soil-air interface) with the thickening of the dry soil layer. In addition, it specifies the minimum vapor conductance at a given thickness of NSL, which occurs when the liquid water saturation in the NSL becomes zero and thus the entire NSL becomes part of the dry soil layer.

2.4. Assembling of the K_{vr} Components

K_{vr} is contributed to by both K_{vr}^c and K_{vr}^v. The K_{vr}^c component dominates at stages II and III but becomes suppressed at stage IV while the K_{vr}^v component takes effect only on stage IV and remains inactivated during stages II and III. Follow the approach of *Brooks and Corey* [1964] in combining capillary water and film water as the compositions of soil water, the expression of K_{vr} can be formulated as:

$$K_{vr} = K_{vr}^c (1 - K_{vr}^v) + K_{vr}^v. \tag{21}$$

Inserting equations (15) and (20) into equation (21) yields

$$K_{vr} = {}_2F_1\left[1, \lambda; 1+\lambda; -\frac{\zeta}{2\delta\Psi_m}\left(\frac{\Psi_m^{\lambda(1+n)}}{\theta_p \Psi_b^{\lambda(1+n)}} - \sqrt{\frac{\Psi_m^{\lambda(1+n)}}{\theta_p \Psi_b^{\lambda(1+n)}}}\right)\right]\left[1 - \frac{\delta \tau_0 \theta_p \ln(-\Psi_0)}{l_0 \ln(-\Psi_m - \Psi_p)}\right] + \frac{\delta \tau_0 \theta_p \ln(-\Psi_0)}{l_0 \ln(-\Psi_m - \Psi_p)}. \tag{22}$$

Equation (22) offers an analytical prediction of the relative vapor conductance through the soil-air interface as a function of matric potential in the NSL. Combing equation (22) and equation (3), one can determine the surface resistance as a function of the matric potential in the NSL. Although the function is not in an explicit form, one can numerically compute the Ψ_m corresponding to the NSL liquid water saturation using equation (5) for given Ψ_b, λ, and Ψ_0, and then use it in equation (22).

3. Laboratory Experiments

3.1. Soil Materials

Three different types of sands were used in the laboratory experiments. Based on the grain size, they were tagged as coarse sand (8/16), medium sand (30/40), and fine sand (30/60). The particle size distributions provided by manufacturers are shown in Figure 4a. The primary drying retention curves of the sands were measured as displayed in Figure 4b. The measurement over the range of liquid water saturation corresponding to matric potential between 0 and −1 m was conducted using a Tempe cell, while the measurement for liquid water saturation corresponding to matric potential from -1×10^2 to -3×10^4 m was undertaken in a chill mirror hygrometer (WP4 dew-point potentiometer, Decagon Device, Inc.). The testing procedure followed the standard of ASTM6836. The properties of the three sands are given in Table 2.

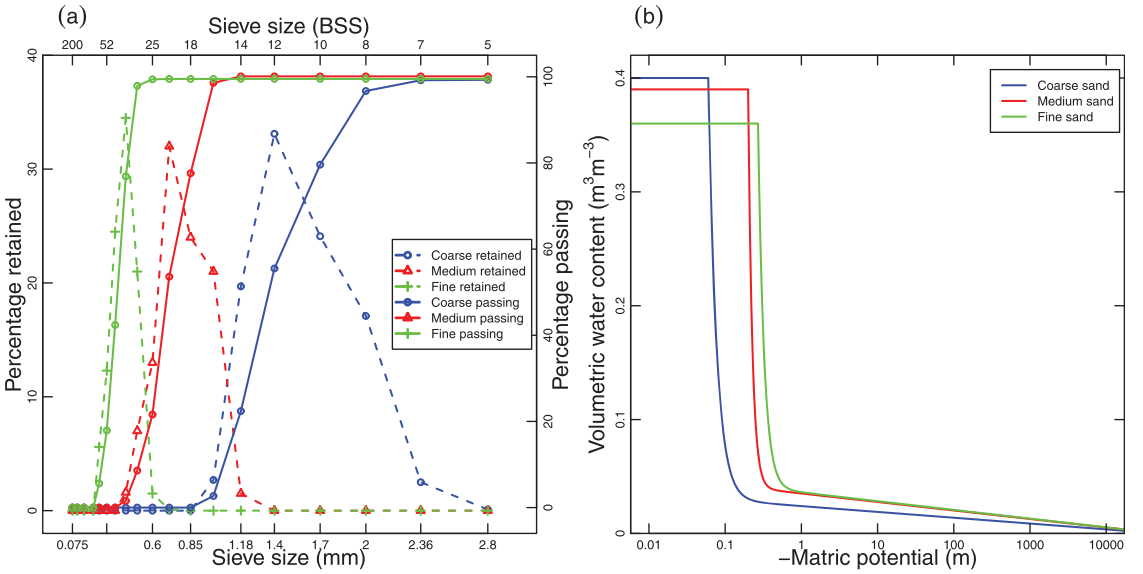

Figure 4. (a) Particle size distribution and (b) water retention curve of the coarse, medium, and fine sands used in the experiments.

3.2. Experimental Apparatus

The experimental setup is shown in Figure 5. A cylindrical column made of acrylic was constructed with horizontal holes perforated on the side for installation of the sensors. The bottom of the column was connected to a water reservoir, which is used to fill the column with the deionized water up above the soil surface. Above the soil column, an infrared lamp (Philips BR125 IR 250W E27 230–250V Red 1CT) with a dimmer switch was installed for supplying heat to the soil surface. During the experiment, the soil column was placed on a scale (Ohaus NVL20000, capacity 20 kg, resolution ± 1 g) for recording the water loss due to evaporation at a 30 s interval. Dielectric soil moisture sensors (ECH_2O EC-5, Decagon Devices, Inc.) were installed at 2 and 8 cm below the soil surface to measure the liquid water saturation. The black handle of each sensor was also buried within the soil, ensuring a good contact of the whole sensor body with the soil [*Sakaki et al.*, 2008]. Dielectric water potential sensors (MPS-2, Decagon Devices, Inc.) were installed at 2 and 8 cm below the soil surface to measure the matric potential and temperature. The dielectric soil moisture sensors were connected to a data logger (DT85G, Thermo Fisher Scientific Australia, Inc.) via analog channels with a 2610 mV external power supply. The dielectric water potential sensors were also connected to the same data logger via SDI12 digital channels. The sensors at the similar elevation were installed from opposing sides to avoid interference. The flat planes of the sensors were placed in parallel to the upward flow direction for the purpose of minimizing the obstruction to flow. Temperature and relative humidity close to the soil surface and 12 cm above the soil surface were monitored by relative humidity sensors (EHT temperature and RH sensor, Decagon Devices, Inc.), which were connected to a second data logger (EM50, Decagon Devices, Inc.). To avoid the black sensor body being directly exposed to the heating source, the relative humidity sensors were covered by a patch of thermal insulator with foam 1 cm thick. All the sensors were set to acquire data at a 15 min interval.

Careful calibrations were conducted on all the sensors before the installation in the column. Dielectric soil moisture sensors were calibrated by inserting the sensors into containers filled by prepared soil samples of

Table 2. Properties of the Testing Sands

Sand Type	Average Particle Size d (m)	Dry Bulk Density (kg m^{-3})	Porosity θ_p	Intrinsic Permeability (m^2)	Brooks-Corey and Fayer Water Retention Model		
					Ψ_b(m)	λ	S_{lr}
Coarse (8/16)	1.4×10^{-3}	2590	0.40	1.00×10^{-9}	0.06	5.0	0.06
Medium (30/40)	0.7×10^{-3}	2604	0.39	5.67×10^{-11}	0.2	8.0	0.09
Fine (30/60)	0.4×10^{-3}	2630	0.36	1.15×10^{-11}	0.27	5.5	0.1

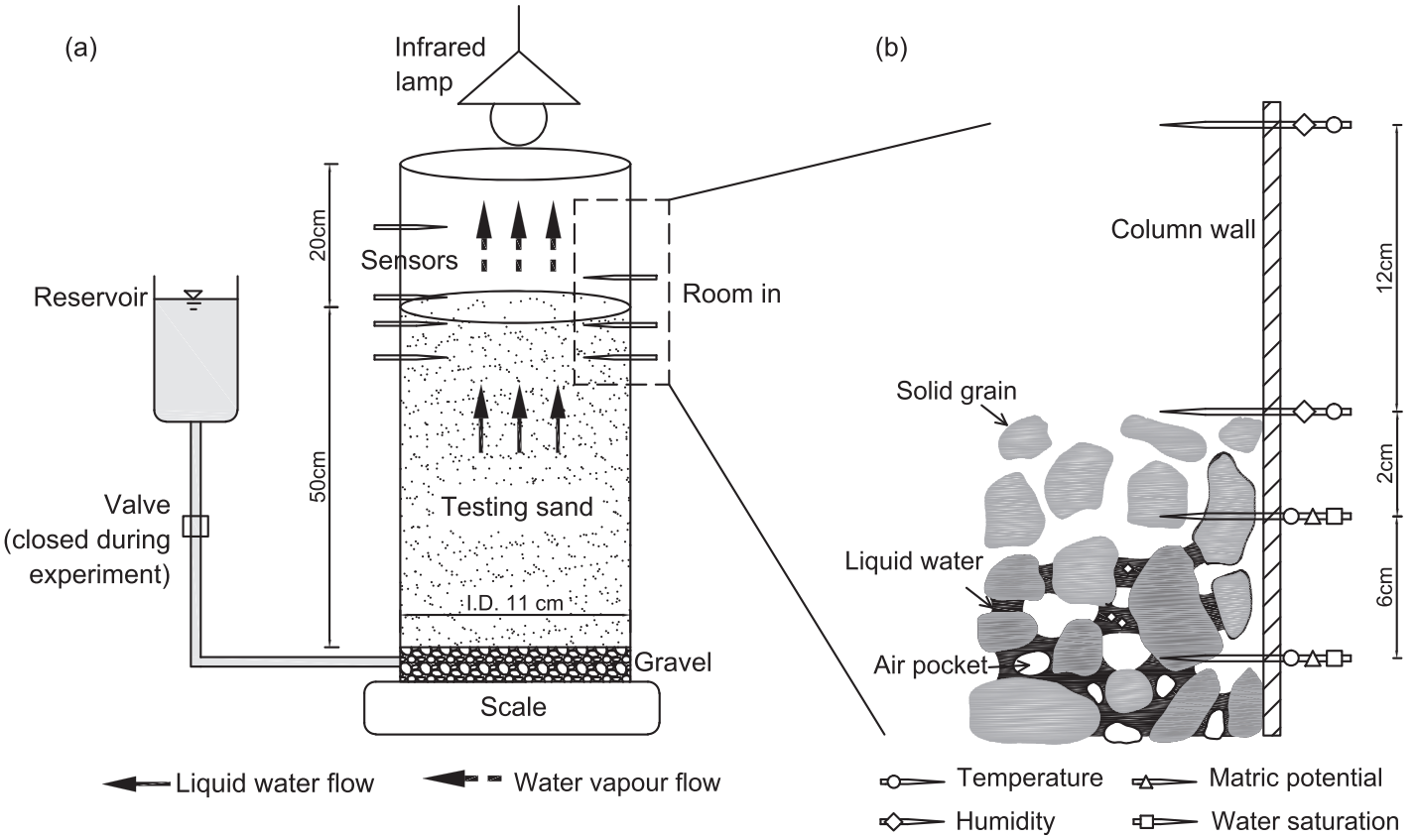

Figure 5. (a) Schematic views of setup of the soil column experiment and (b) enlarged view of the soil-air interface. Note that the sensors in Figure 5b only show the elevations at the centerline of the sensors. The figure is not drawn to scale.

which the liquid water saturation and porosity were known. The two-point method proposed by *Sakaki et al.* [2008] was applied and found to fit well with the correlations between the liquid water saturation and output voltage from dielectric soil moisture sensors responding to all the sands. Tests on the sensitivity of output voltage to soil temperature were also conducted. Higher soil temperature was found to result in only slightly lower output voltage for the same liquid water saturation, causing relatively small errors ($<$2%) over the temperature range from 20°C to 60°C. Intercalibration tests were conducted among the dielectric water potential sensors and relative humidity sensors by comparing the readings after placing them in the same environment.

The dielectric moisture sensor near the surface was placed as close to the surface as possible so that the thickness of NSL corresponding to the sensor readings can be thin. However, if the sensor is too close to the surface, the obtained liquid water saturation can be affected by the ponding water above the soil surface during stage I. Although *Sakaki et al.* [2008] suggested an effective sensor measurement distance of 2 cm, our tests showed that if placed 1 cm below the soil surface, the sensor would give readings affected little by the ponding water, with measured liquid water saturation equal to 1. According to the dielectric moisture sensor reading, the thickness of the NSL is 5 cm: 1 cm above, 2 cm below the sensor body, and 2 cm for the width of the sensor face.

3.3. Experimental Procedure

The experiment was conducted in an environmentally controlled laboratory with temperature 22°C and relative humidity 50%. Gravels were first packed over a 5 cm thickness at the bottom of the column to enhance the hydraulic connectivity between the bottom of the testing sand and reservoir. A circular metal wire mesh with 0.3 mm openings wrapped by geotextile was placed between the gravel and sand above to prevent sand from mixing with gravels without losing the hydraulic connection. Sensors were then installed from the side of the column prior to sand packing. Following *Smits et al.* [2011], sand

Table 3. Evaporation Rate and Parameters Applied in Each Experimental Case

Cases	Maximum Evaporation Rate (mm d^{-1})	Constant Evaporation Rate at Stage II (mm d^{-1})	Evaporation Rate at Stage IV (mm d^{-1})	Aerodynamic Resistance (s m^{-1})	n	δ (mm)	Ψ_p (m)
C9	9.42	5–8	0.9–1.1	140.16	0.5	1.0	−10
C4	4.41	3.5–4.0	0.7–1.1	180.80	0.5	3.5	−10
M14	14.11	10–11	1–1.2	96.19	0.5	1.5	−5
M7	6.73	5.5–6.0	0.4–2	129.03	0.5	1.4	−5
F10	10.14	4.5–6.5	1–0.8	129.60	0.5	4.0	−10
F6	5.57	3.5–4.5	1.5–2	132.59	0.5	6.0	−10

packing was done by iteratively pouring 2 cm thick dry sand and then tapping the column wall to achieve uniform bulk density across the column while ensuring the integrity of sensor networks. The packed sand in the end was 50 cm in depth with a 20 cm distance from the soil surface to the opening top of the column where the infrared lamp locates. The 20 cm tunnel above the soil surface ensures that the vapor flow regime in the air is 1-D and not disturbed significantly by the ambient airflow in the laboratory.

After switching on the valve between the column and water reservoir, water gradually filled the column from the bottom up above the soil surface. Through this method, the problem with entrapped air bubbles in the pore space could be avoided or minimized. The column was then placed still for 1 day to reach an equilibrium condition. The experiment started with the valve to the reservoir closed and the infrared lamp switched on. The experiment continued until the evaporation rate became very low. The experiment was then repeated with different heat intensities and/or soil types. Six cases were conducted using three soil samples (Table 3). They are tagged as C9, C4, M14, M7, F10, and F6. The capital letters refers to soil type (C for coarse sand, M for medium sand, and F for find sand) and the number refers to the maximum evaporation rate in mm d^{-1}.

3.4. Data Processing

The cumulative evaporation was obtained by deducting the scale reading at the measurement time from the initial reading at the beginning of the experiment. The evaporation rate was then obtained by calculating the derivative of the cumulative evaporation with respect to time using a finite difference method (FDM). To reduce the noise in the calculated evaporation rate, a cubic spline interpolation (CSI) of the cumulative evaporation data was carried out before applying the FDM.

Using data measured in the NSL and at the reference point as well as the evaporation rate obtained from the scale, we can calculate the surface resistance r_s (s m^{-1}) [*Van de Griend and Owe*, 1994]:

$$r_s = \frac{\rho^*_{v\mathrm{NSL}} - \rho_{v\mathrm{Ref}}}{\rho_l E} - r_a. \tag{23}$$

The reference point was chosen at 12 cm above the soil surface where the topmost relative humidity sensor is located. Obtaining the surface resistance using equation (23) requires the aerodynamic resistance r_a (s m^{-1}), which represents the resistance of vapor through the air up to the reference point. This resistance is obtained by inverse calculation based on equation (23) using data collected at the beginning of each experiment when the surface resistance equals to zero under the water ponding condition, i.e.,

$$r_a = \frac{\rho^{*\mathrm{Int}}_{v1} - \rho^{\mathrm{Int}}_{v\mathrm{Ref}}}{\rho_l E^{\mathrm{Int}}}. \tag{24}$$

The superscript int refers to the initial values for each experimental case. Since the aerodynamic regime remains undisturbed and constant during the experiment, the aerodynamic resistance obtained by equation (24) is assumed to remain constant throughout each experiment [*Van de Griend and Owe*, 1994]. The obtained aerodynamic resistance for each case is listed in Table 3.

It is also noted that calculating the surface resistance at a particular time by equation (23) requires the temperature, liquid water saturation in the NSL, and the evaporation rate at the same time. However, these properties were measured by different equipment acquiring data at different time intervals. This problem can be resolved by interpolating the measured properties for the desired time.

4. Results Analysis

Figure 6 displays the data collected for case M14. At stage I when water was ponding above the soil surface, the relative humidity above the soil surface remained relatively constant with a downward gradient. The temperature in the soil and air above the soil surface rose immediately after the experiment started and then remained relatively constant during stages I and II. The evaporation rate dropped steadily from the initial, maximum value measured at the beginning of the experiment. At stage II, the evaporation rate remained comparably constant, while the liquid water saturation in the NSL decreased considerably. At later stage II, the liquid water saturation at 8 cm below the surface began to fall. During stage III, the evaporation rate started to decline quickly. In the same time, the relative humidity measured above the soil surface also decreased significantly. Slight increase of the temperature above the soil surface was also observed during stage III. At stage IV, the evaporation rate was low and decreased gradually over time. The temperature and humidity also remained relatively unchanged.

The fitted cumulative evaporation by the CSI method only filters out the noise in the raw data, which gets magnified when the time derivative is calculated. In other words, the fitting does not alter the information in the data (Figure 6d), including the first-order derivative with respect to time (evaporation rate; Figure 6e).

4.1. Comparison Between Experimental and Model Results

Figure 7 displays the comparison of surface resistances obtained by the experiment and model for all cases. According to the experimental results, the variations of surface resistances with respect to the liquid water saturation in the NSL follow a similar trend; specifically, the resistance value equals zero at the full liquid water saturation, then slightly goes up to around 100 m s^{-1} over the high liquid water saturation range (0.5–1), after that remains relatively constant for the intermediate liquid water saturation range (0.2–0.5), and lastly rises drastically to a high value when the liquid water saturation is low. For cases using the same soil type, the results show that in the high liquid water saturation range, the cases with lower potential evaporation resulted in greater surface resistance. In the low liquid water saturation range, the variations in the potential evaporation rate led to little difference in the surface resistance.

The proposed model (combining equations (3) and (22)) used the measured liquid water saturation and temperature in the TSL as inputs to produce the predictions. Following the study of *Shokri and Or* [2011] in which the jumping length of the dry soil layer was found to depend on the soil grain sizes, the value of Ψ_p was assumed to vary only with soil types. For the cases with the same soil type, the variations of the potential evaporation rate were achieved by changing the δ values. With the same liquid water saturation, higher potential evaporation rate results in lower δ, which leads to lower surface resistance. This is consistent with the results of *Shahraeeni et al.* [2012] who found greater potential evaporation rate induced by stronger wind above the evaporating soil surface leading to lower δ. However, no consistent δ relation could be found among different soil types.

The model predictions agree well with experimental results in the medium and low ranges of liquid water saturation (Figure 7). However, notable deviations occur in the high liquid water saturation range (0.8–1); in particular, the surface resistance predicted by the model starts from a nonzero value at the full liquid water saturation followed by relatively constant values in the medium and high liquid water saturation ranges (0.2–1). The overestimation of the resistance at the full liquid water saturation is due to the fact that the model does not describe the connectivity between capillary water in the pore and film water adjacent to it. At the full liquid water saturation, the film water around the soil grains facing the air remains thick and hence maintains a good hydraulic connection with capillary water in the pore. As a result, vaporization may occur not only from the capillary water surface, but also from the film water surface with abundant capillary water supply from pores. Therefore, evaporation from soil in high liquid water saturation behaves similarly to that from free water surface. In contrast, with no vapor flux applied perpendicular to the soil grain surface in the model, vapor generated from all the pores has to diffuse from pore surface to the entire soil surface described by equation (7). This results in the prediction of a nonnegligible resistance, unrealistically present at the full liquid water saturation.

The increase of resistance at the early desaturation stage during the experiment might be caused by both the air invasion to the pores and the weakening of hydraulic connection between the capillary water and film water. Given that the model considers only the former and hence failed to predict the rise of resistance,

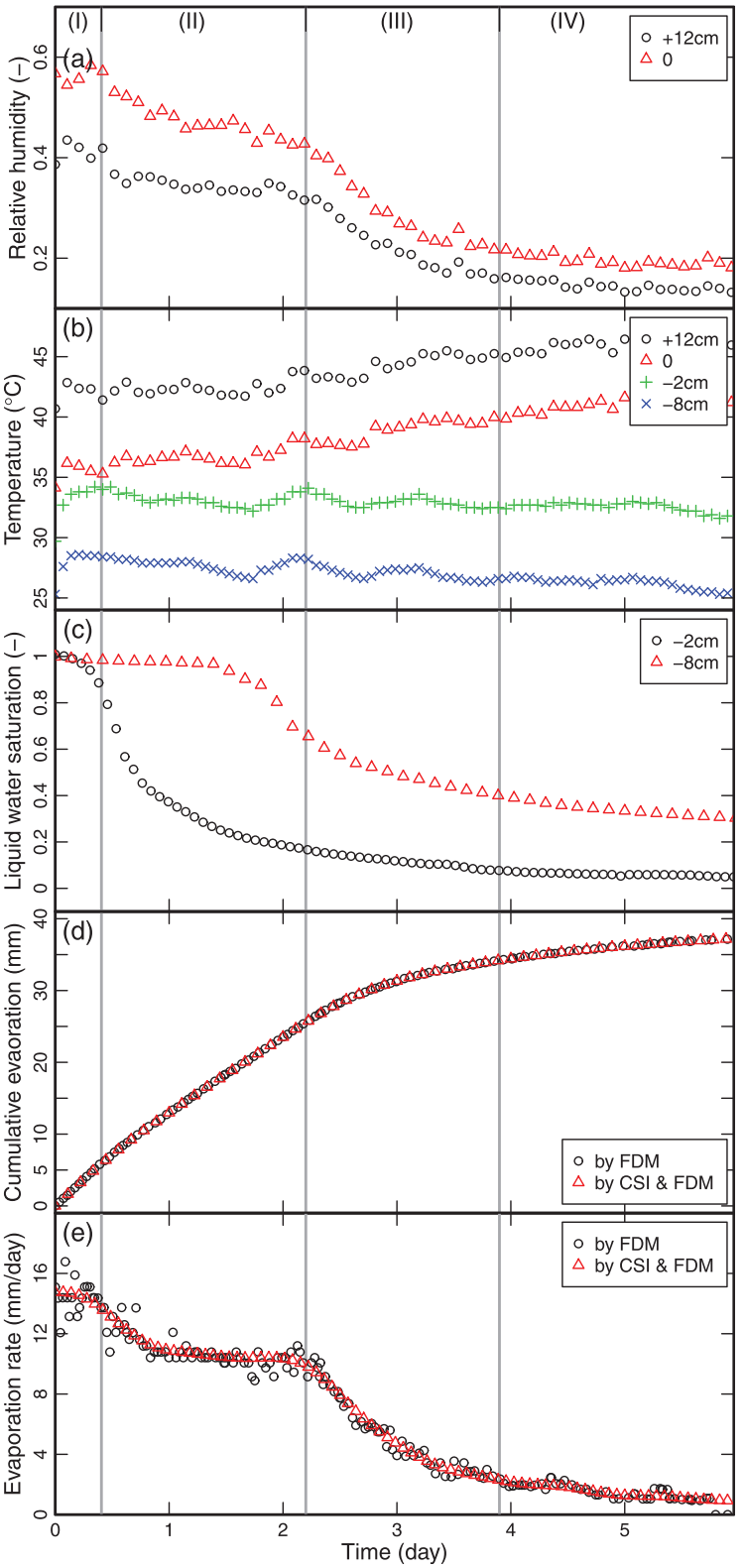

Figure 6. Data collected for case M14, including (a) relative humidity, (b) temperature, (c) liquid water saturation, (d) cumulative evaporation, and (e) evaporation rate. The four evaporation stages are identified by gray lines. The elevation specified in the legend is the distance from the soil surface to the centerline of the sensor (positive upward). The liquid water saturation at −2 cm represents the saturation condition in the NSL (5 cm thickness).

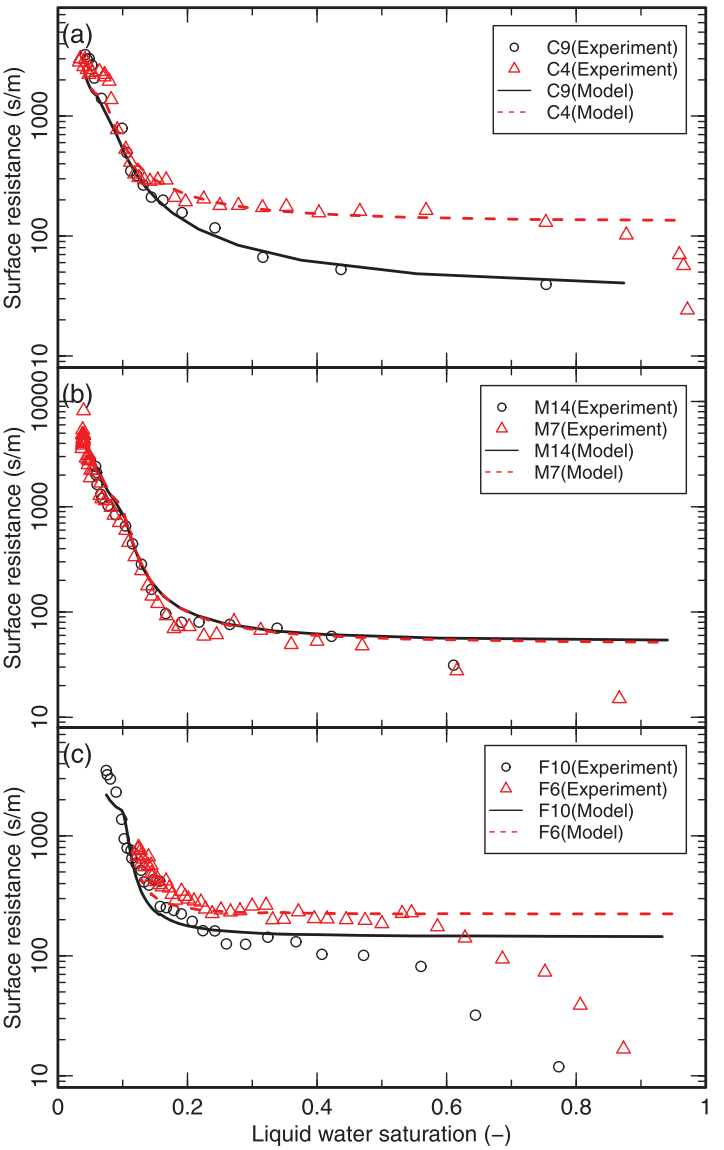

Figure 7. Comparisons of surface resistance as a function of liquid water saturation obtained by reverse calculation from experiments (shapes) and proposed model (lines). The time interval between two neighboring data points is 6.67 h.

it is speculated that the vaporization of capillary water from film water surface plays an important role in the high liquid water saturation range. The soil particle size may also affect the hydraulic connection between capillary water and film water as the film water in the finer soil may have better chance of gaining capillary water supply from neighboring pores, which would lead to a larger vaporization surface. The comparison of resistances estimated from the experimental results and predicted by the model confirms the relationship between the hydraulic connection and soil particle size. Finer soil tends to obtain consistency between the experimental and model results at relatively lower liquid water saturation (coarse sand cases occurred at 0.9 in Figure 7a, medium sand cases occurred at 0.6 in Figure 7b, and fine sand cases occurred at 0.5 in Figure 7c).

Although the surface resistance predicted by equation (3) is dependent on the temperature in the TSL, the results do not show significant fluctuations due to minor oscillations of the measured temperature in the TSL.

Figure 8 displays the comparison of the evaporation rate as a function of the liquid water saturation in the NSL. Except for the underestimation over the high liquid water saturation range, the evaporation rates

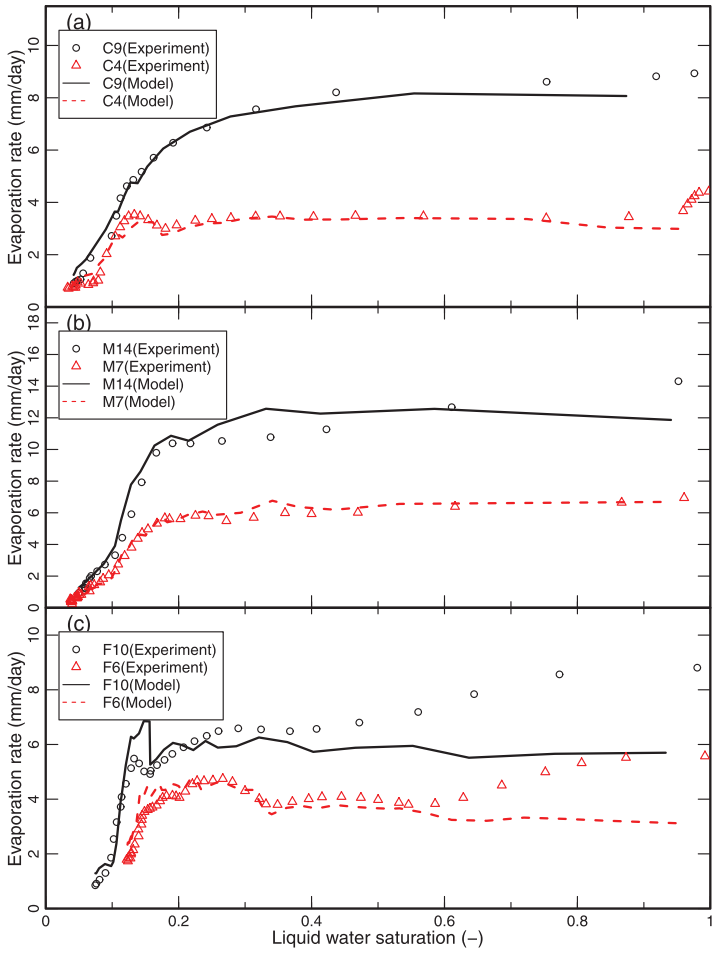

Figure 8. Evaporation rates versus the liquid water saturation in the NSL. Results obtained by experiments are indicated by symbols and model predictions plotted by lines. The time interval between two neighboring data points is 6.67 h.

calculated using the surface resistance predicted by model generally agree well with those measured during the experiments. The underestimation of the evaporation rate is directly linked to the overestimation of the surface resistance in the high liquid water saturation range (Figure 7). Although notable discrepancies in surface resistance can be identified for both medium and fine sand cases in the high liquid water saturation range (Figures 7b and 7c), the difference between the evaporation rate predicted by the model and that from the experiment is small for the medium sand cases (Figure 8b) but relatively large for the fine sand cases (Figure 8c). This is due to the fact that the surface resistance in the high liquid water saturation range is lower (less than 100 s m^{-1}; Figure 7b) in the medium soil cases than that in the fine soil cases (greater than 100 s m^{-1}; Figure 7c).

Different from the surface resistance, the evaporation rate obtained through the model shows notable fluctuations owing to the oscillations in the measured temperature in the NSL. This implies that although surface resistance is not sensitive to the change of temperature in the TSL, good estimations of the evaporation rate still require accurate temperature measurements in the NSL. For example, the overestimation of the evaporation rate in case F10 near the residual saturation (Figure 8c) is not attributed to the discrepancies in the surface resistance (Figure 7c), but to the relatively high temperature measured during that period (probably produced by measurement errors). Similarly in case C4, the slight rise of the evaporation rate before a sharp fall (Figure 8a) is not induced by the decrease of the surface resistance but by the rise of the temperature.

The comparison of the evaporation rate over time between the experimental results and model predictions is illustrated in Figure 9. The initial time (=0) is set when water is ponded above the soil surface. As it is

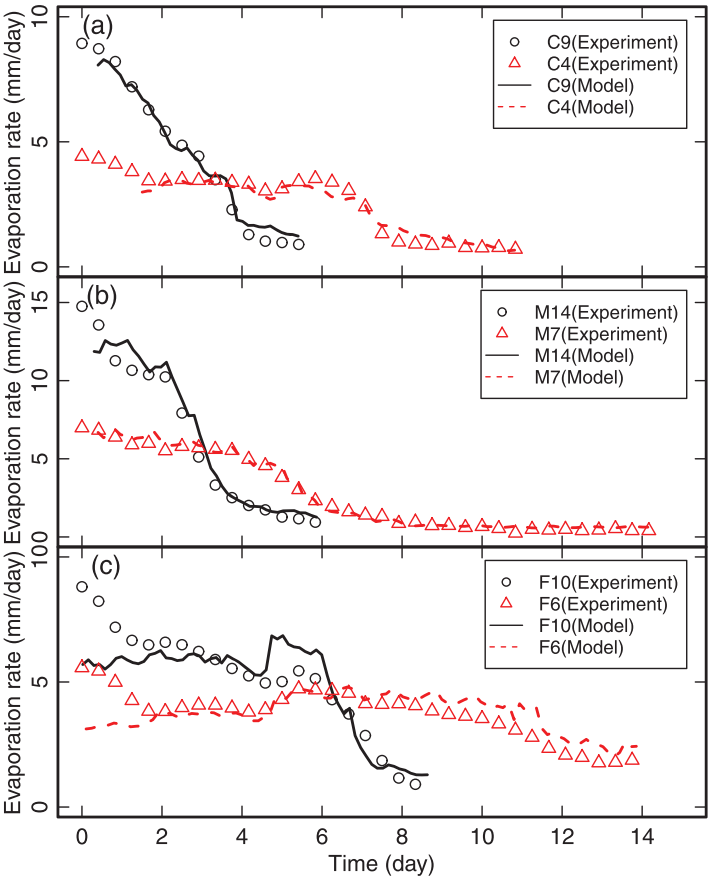

Figure 9. Evaporation rate versus time: results obtained from experiments (symbols) and model (lines). The time interval between two neighboring data points is 6.67 h.

incapable of describing the water level receding until soil grains emerged in stage II, the model starts to make predictions from the commencement of stage II as indicated by the desaturation of the NSL and the decrease of the relative humidity above the soil surface. Despite the deviation of the resistance in the high liquid water saturation range, the resultant underestimation of the evaporation rate at early stage II is not apparent in the coarse and medium sand cases, but evident in the fine sand cases. This is because under the same matric potential, fine sand can maintain higher liquid water saturation than medium and coarse sand (Figure 4b), which leads to longer duration of high liquid water saturation in the NSL and hence more pronounced difference between the experimental and modeling results.

To illustrate the overall performance of the model, Figure 10 displays the evaporation rate varying with the cumulative evaporation. To start from the same time point as the model, water evaporated during stage I in the experiment is deducted from its cumulative evaporation. For the same soil type, stage IV starts after the same amount of water loss by the evaporation rate (20 mm for coarse sand, 33 mm for medium sand, and 45 mm for find sand). Although slight underestimation (case C4) and overestimation (cases M14 and M7) occur at the end of the experiment, the maximum discrepancy is around 10% (for case M14). For the fine sand cases, a balance appears to exist between the underestimation at early stage II and slight overestimation for the rest of stages; thus, the cumulative evaporation prediction matches well the experimental result at the end of the experiment/simulation.

4.2. Sensitivity Analysis and Model Comparisons

Besides requiring the parameters describing the soil hydraulic properties in the NSL (e.g., θ_p, Ψ_0, λ, Ψ_b, and Ψ_m), which is needed by other surface resistance models, the proposed model also requires the inputs of the other parameters describing the thickness of the EDL δ and the NSL l_0, correction function G (specifically the exponent parameter n), and the threshold matric potential in the NSL where MCD occurs Ψ_p. This

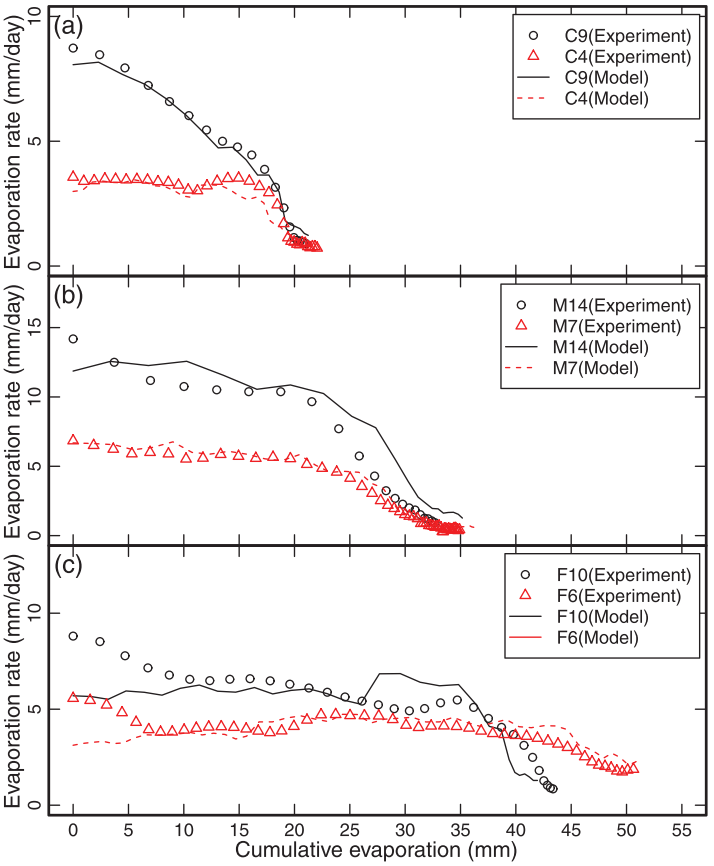

Figure 10. Evaporation rate versus the cumulative evaporation: results obtained from experiments (symbols) and model (lines). The time interval between two neighboring data points is 6.67 h.

section focuses on the sensitivity analysis of the parameters not associated with soil hydraulic properties. In addition, the surface resistance and evaporation rate predicted by other surface resistance models are presented.

As discussed in section 4.1, the effect of δ on the surface resistance and the evaporation rate can be distinguished between different cases using the same soil type. Although larger δ results in greater surface resistance at the same liquid water saturation, the difference becomes small in the low liquid water saturation range (Figures 7 and 9).

To explore the effect of the correction function *G*, the model was applied case C9 with different values of the exponent parameter *n* (involved in the *G* function as expressed by equation (6)). The results (Figure 11) show that varying the value of *n* does not affect the results of surface resistance or evaporation rate in the low liquid water saturation range (0 to residual saturation). However, a greater *n* value produces higher surface resistance in the medium and high liquid water saturation range (from residual saturation to 1), which in turn leads to lower evaporation rates during stages II and III. Figure 11 also reveals that without considering the correction function *G* ($n = 0$), the surface resistance by the model is significantly underestimated, leading to overestimation of the evaporation rate.

Figure 11 also presents the results by the *Schlünder*'s [1988a] model and an empirical-based model by *Van de Griend and Owe* [1994]. The surface resistance used in the *Schlünder*'s [1988a] model is given by:

$$r_s = \frac{\delta}{D_v}\left[1+\frac{2r_{avg}}{\pi\delta}\sqrt{\frac{1}{4\theta_{INSL}}}\left(\sqrt{\frac{\pi}{4\theta_{INSL}}}-1\right)\right], \tag{25}$$

where $r_{avg} = \int_0^{r_b} rf(r, r_b)dr$ (m) is the average pore radius. The empirical-based model by *Van de Griend and Owe* [1994] is as follows:

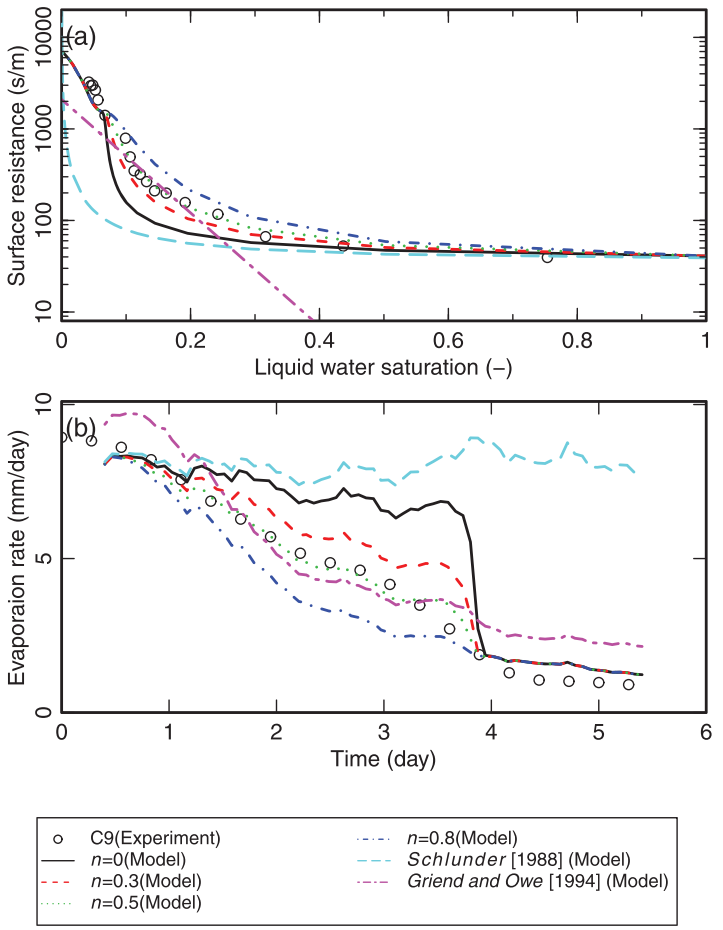

Figure 11. Comparisons of (a) the surface resistance and (b) the evaporation rate obtained by the model using different *n* values for case C9. The experimental results are also displayed by symbols.

$$r_s = 10\exp[35.63(0.15-\theta_{INSL})]. \quad (26)$$

The *Schlünder*'s [1988a] model underestimates the surface resistance at the low liquid water saturation, which results in significant overestimation of the evaporation rate at stages II, III, and IV. This discrepancy, as described in section 1, is due to both the neglect of the connectivity between water-saturated pore in the TSL and the MWC underneath, and the misrepresentation of evaporation contributed to by film water. The *Van de Griend and Owe*'s [1994] model underestimates the surface resistance during stages II and IV, which leads to the overestimation of the evaporation rate in these two stages. The underestimation of surface resistance during the stage IV may be attributed to the thickness of the NSL used in their study. Specifically, the NSL in their study, set to 0.5 cm in thickness and corresponding to a maximum surface resistance of 2000 s m^{-1} (when the entire NSL is dried), is thinner than the NSL used in this study (4 cm in thickness and corresponding to 7000 s m^{-1} maximum surface resistance). One may not be able to adjust the thickness of the NSL using *Van de Griend and Owe*'s [1994] model due to lack of the physical basis.

The effect of Ψ_p on model results for case M7 is shown displayed in Figure 12. Varying Ψ_p does not affect the maximum surface resistance and hence the evaporation rate at stage IV. Smaller Ψ_p leads to a wider transition section between the residual saturation and the liquid water saturation corresponding to Ψ_p. The surface resistance in the transition section is relatively constant, which is consistent with the jumping length of the vaporization plane during the MCD. Such a transition section is evident in the experimental cases (e.g., case C4, M14, and M7 shown in Figure 7). Above the residual liquid water saturation (0.09 for medium sand), the resistance is predominantly associated with the vaporization of capillary water in the TSL. Below the liquid water saturation corresponding to Ψ_p, the resistance is linked with diffusion of vapor generated from the vaporization plane below the TSL. Apart from lengthening the

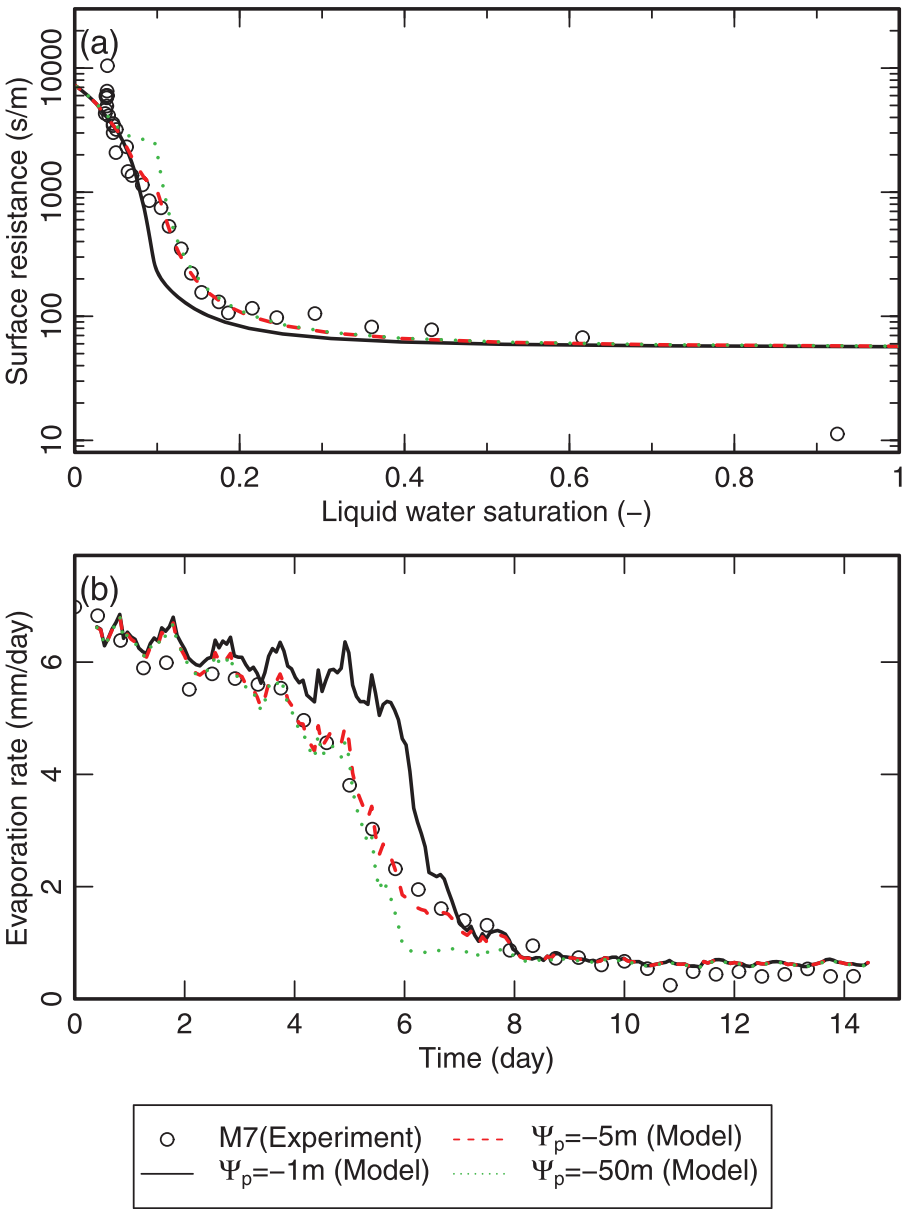

Figure 12. Comparisons of the (a) surface resistance and (b) evaporation rate obtained by the model using different Ψ_p values for case C9. The experimental results are also displayed by the symbols.

transition section, smaller Ψ_p also results in the thicker jumping length of the vaporization plane, which leads to a greater surface resistance at the transition section and lower evaporation rate during stage III and MCD.

In the model, the thickness of NSL l_0 is also a key parameter. Figure 13 displays the variations of surface resistance and evaporation rate predicted for case F10 using different l_0 values. l_0 does not change the increasing trend of surface resistance with the soil desaturation at stage IV. Larger l_0 leads to higher surface resistance at the beginning of stage IV and increases the maximum surface resistance as the liquid water saturation in the NSL approaches zero. Note that the jumping length does not depend on the evaporation intensity or the thickness of NSL where the liquid water saturation is measured, but is intrinsic to the soil types [*Shokri and Or*, 2011]. This suggests that if l_0 is varied due to, for example, the change of equipment that measures the liquid water saturation in the NSL, one should adjust the value of Ψ_p so that the same jumping length is maintained for a particular soil.

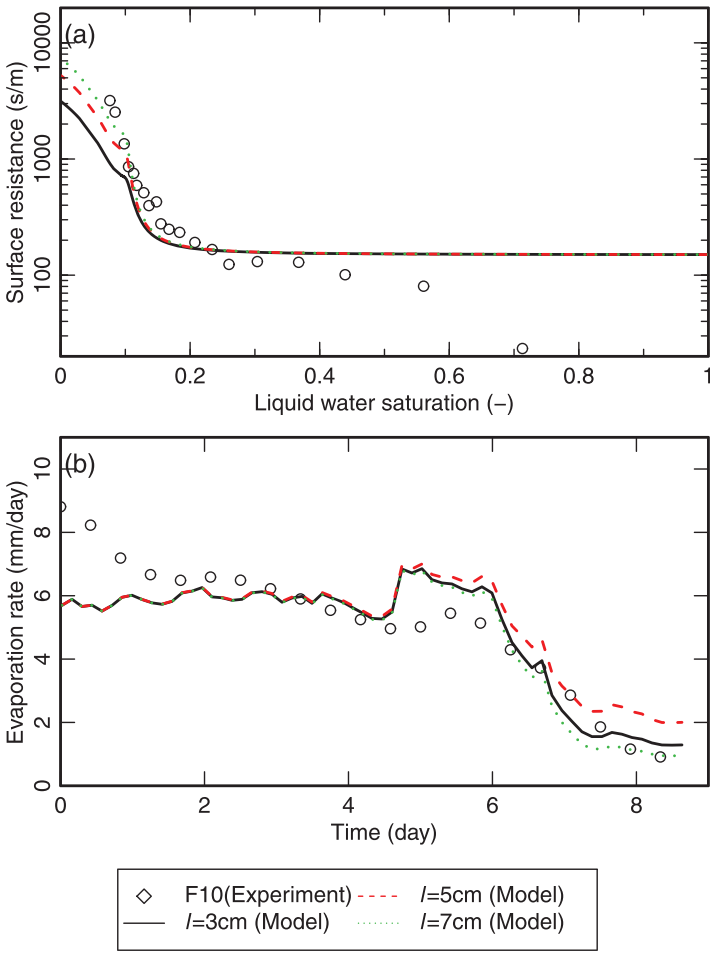

Figure 13. Comparisons of the (a) surface resistance and (b) evaporation rate obtained by the model using different l_0 values for case F10. The experimental results are also displayed by symbols.

5. Discussion on the Model Assumptions

5.1. Correction Function

The introduction of the correction function *G*, as discussed in section 2, is due to the discrepancy of the volumetric water content in the NSL and that in TSL (referred to as factor (1)). There are other factors that need to be considered by the correction function in the model: (2) the roughness of the soil surface; (3) the interaction of neighboring water-saturated pores resulting from the multiplicity of pore shapes and spacing [e.g., *Cooke*, 1967; *Parlange and Waggoner*, 1970]; (4) the nonequilibrium condition between the matric potential and the saturated vapor pressure (equilibrium assumed by the Kelvin equation) [*Smits et al*., 2011]; and (5) the permeability of liquid water through the water-saturated pores in the TSL. It appears that the factors (1), (4), and (5) may become more significant with the decrease of water saturation, while factors (2) and (3) may be less important once the soil becomes dry [e.g., *Cooke*, 1967; *Parlange and Waggoner*, 1970]. Although it is not clear which factors outweigh others as model does not physically describe these effects, a power function of effective liquid water saturation in the NSL appears to describe the lumped effects of these factors, according to the model validation results. This correction function happened to resemble the correction function used by *Mualem* [1976] for describing the effects of tortuosity and eccentricity on liquid water permeability.

5.2. Vapor Transport Through the Air-Invaded Pores in the TSL

During stages II and III, the model assumes that evaporation is only contributed to by the vaporization of capillary water from the water-saturated pores in the TSL, with the possible contribution of vapor from the

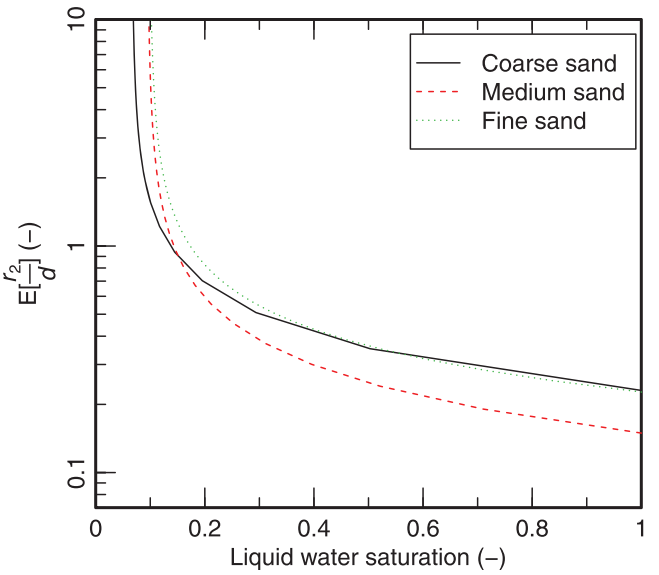

Figure 14. Expected value of ratio of r_2 to d as a function of the liquid water saturation in the NSL.

air-invaded pores neglected. However, as shown in Figure 2c, if the air-invaded pores in the TSL is connected to a water-saturated pore at the soil layer underneath the TSL (e.g., 1@1 in Figure 2c), vapor may be transported through that air-invaded pores, thus contributing to evaporation. The validation of such assumption will be discussed at both macroscopic and microscopic scales.

Over the soil column, the matric potentials at a certain elevation are the same at the macroscopic scale. Under the assumption of equilibrium between liquid water and vapor, the vapor densities of the air-invaded pores at a certain elevation are also the same as specified by the Kelvin equation (Table 1). Since the vapor transport in the soil is dominated by diffusion [*Smits et al*., 2011], the vertical vapor flux (positive upward) q_v (m s^{-1}) can be expressed by:

$$q_v = -D_v \tau \theta_a \frac{\partial \rho_v^* h_r}{\partial z} = -D_v \tau \theta_a \left(\eta h_r \frac{\partial \rho_v^*}{\partial z} + \rho_v^* \frac{\partial h_r}{\partial z} \right), \tag{27}$$

where z (m) is the vertical coordinate (positive upward) and η (−) is the enhancement factor of vapor proposed by *Philip and De Vries* [1957] for describing the intensified vapor flow under thermal gradients. It is known that based on the Kelvin equation, the relative humidity remains nearly unity when the matric potential is greater than -1×10^2 m. However, if the matric potential equals -1×10^2 m, the corresponding liquid water saturation of the soils applied in this study has fallen below the residual liquid water saturation. This suggests that in the unsaturated zone, the vapor transport is not driven by the gradient of the relative humidity (the second term on the rightmost hand side of equation (27) approaches 0), but dependent on the gradient of ρ_v^*. Given that ρ_v^* is a monotonically increasing function of temperature (Table 1) and the gradient of temperature in the soil is upward, the direction of the vapor flow is actually downward. Along with the upward liquid water flow driven by evaporation, there is a water circulation taking place in the unsaturated zone below the vaporization plane: liquid water converts into vapor phase at the vaporization plane, then transports downward driven by temperature gradients, condensates into the liquid phase in the unsaturated zone below the vaporization plane, and then flows upward due to the gradient of matric potential. However, the vapor moving downward does not disrupt evaporation as the upward liquid water transport dominates.

One may also argue that under the microscopic scale such as that based on the pore bundle concept sketched in Figure 2c, using the Kelvin equation to describe the vapor density at the air-invaded pore in the TSL may not be valid. Rather than a constant vapor density, downward gradient of vapor density exists in the air-invaded pores as water only present at the bottom of the TSL (e.g., 1@1 in Figure 2c). To reconcile this issue, one may compare the radius of the sphere that cover the surface of building block r_2 and the thickness of the TSL d to determine the preferential path for vapor transport up to the sphere that covers the whole building block (Figure 2c). The expected value of r_2/d at a given matric potential Ψ_m can be calculated by combining equations (4), (5), and (14b):

$$\mathrm{E}\left[\frac{r_2}{d}\right] = \int_0^{r_m} \frac{r_2}{d} f(r_1) dr_1 = \frac{\lambda \zeta}{(\lambda+1) d \Psi_m} \sqrt{\frac{{\Psi_m}^{\lambda(1+n)}}{\theta_p {\Psi_b}^{\lambda(1+n)}}}. \tag{28}$$

As shown in Figure 14, the ratio of r_2 to d rises up to 1 when the liquid water saturation in the NSL is approximately 0.2. This implies that liquid water is preferably vaporized from the water-saturated pores in

the TSL rather than that underneath the TSL. Although d becomes larger than r_2 at a lower liquid water saturation, the MWC may have already receded down further to the deeper soil layers rather than the layer beneath the TSL. It is worthwhile to point out that the ratio of r_2 to d would increase if the water permeability through the water-saturated pores is considered; however, the effect of water permeability on the ratio of r_2 to d may be minimal for sand in the large liquid water range as large particle size results in large pore size, which leads to high water permeability in the water-saturated pores. Therefore, it is reasonable to assume that unless the hydraulic connection between the TSL and the MWC is disrupted, vaporization preferentially takes place at the water-air interface of the capillary water in the TSL.

6. Concluding Remarks

An analytical model for predicting the surface resistance to vapor transport through the soil-air interface during the soil-drying process has been developed. This model incorporates the description of the water transport in liquid water and vapor phases through both the NSL and the EDL above the soil surface. Specifically, when the vaporization plane remains in the TSL, the model describes the surface resistance with consideration of the vapor transport through the EDL as well as the hydraulic connection between the capillary water in the TSL and MWC underneath the TSL. When the vaporization plane develops below the TSL, the model estimates the thickness of the dry soil layer in the NSL and incorporates it in the determination of the surface resistance.

The model is validated through applications to estimate the surface resistance and evaporation rate for six experimental cases focusing on the drying process of initially water-saturated soil columns. These experimental cases differ from each other by varying soil types and/or the heat intensities from the soil surface. The model performs well in the intermediate and low liquid water saturation range, while overestimating the surface resistance for high liquid water saturation and before the soil desaturation. The theoretical considerations of the model together with its performances in estimating the surface resistance for the laboratory experiments indicate that (1) water is preferentially evaporated from capillary water in the TSL rather than from water in the soil layers underneath the TSL when the vaporization plane is in the TSL; (2) the hydraulic connection between the capillary water in the TSL and the MWC underneath plays an important role in determining the active pores in the TSL that supply capillary water for evaporation; (3) the considerations of the soil pore size distribution facilitate the model applications to different soil types; and (4) determining the thickness of the dry soil layer is essential for properly estimating the evaporation rate at stage IV.

Further research work should be focusing on incorporating the effects of water level recession, soil grains emergence before soil desaturation, the inclusion of salt, clay or organic matters in soils, and the connectivity between capillary water and neighboring film water in the TSL for high liquid water saturation on the surface resistance to improve the performance of the model at the early stage of the soil-drying process.

Appendix A: Closed-Form Approximation of K_{vr}^c

In section 2.2, K_{vr}^c is obtained by calculating the expected value of k_{vr}^c according to the PDF of water-saturated pores at a given matric potential Ψ_m (this approach is called the original approach hereafter). This original approach can be approximated by replacing r_1 in equation (12) with the expected value of the water-saturated pore size $\mathrm{E}[r_1]$ at a given matric potential Ψ_m (called as the approximated solution hereafter). Based on the soil water retention curve by *Brooks and Corey* [1964], $\mathrm{E}[r_1]$ can be calculated as:

$$\mathrm{E}[r_1]=\int_0^{r_m} r_1 f(r_1,r_m)dr_1=\int_0^{r_m} r_1\lambda\left(\frac{\Psi_m}{\zeta}\right)^{\lambda} r_1^{\lambda-1}dr_1=\frac{\lambda r_m}{(\lambda+1)}. \tag{A1}$$

Replacing r_m in equation (12) with $\mathrm{E}[r_1]$ leads to an approximate formulation of K_{vr}^c:

$$K_{vr}^c \approx \frac{1}{1+\frac{\zeta\lambda}{2\delta\Psi_m(\lambda+1)}\left[\frac{\Psi_m^{\lambda(1+n)}}{\theta_p\Psi_b^{\lambda(1+n)}}-\sqrt{\frac{\Psi_m^{\lambda(1+n)}}{\theta_p\Psi_b^{\lambda(1+n)}}}\right]}. \tag{A2}$$

A closed-form expression of surface resistance can be obtained by combining equations (3), (20), (21), and (A2). Figure A1 shows the comparison of surface resistance based on the original solution and

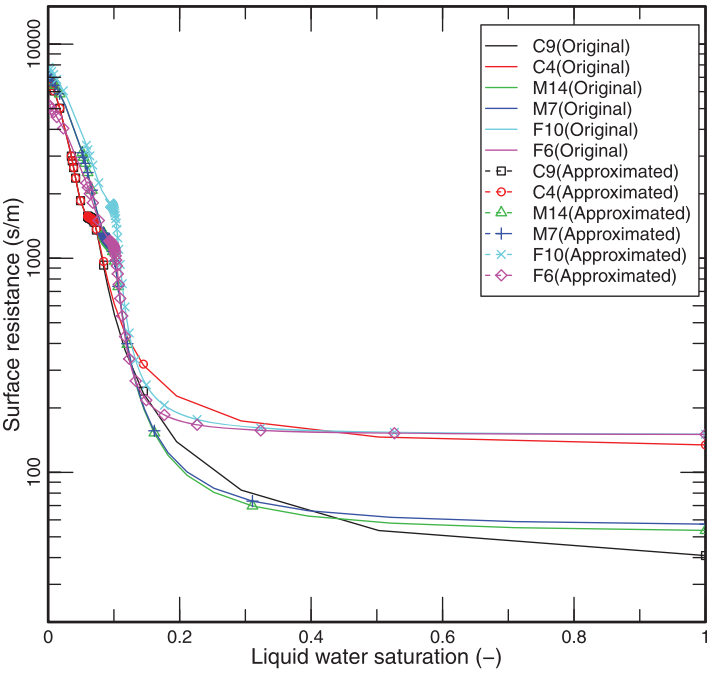

Figure A1. Surface resistances of the six experimental cases predicted by the original solution (equation (22)) and the approximate solution (by combining equations (3), (12), (20), (21), and (A2)). The two solutions are found to largely overlap.

approximated solution for all the cases considered in this study. Results show that the approximate solution matches the original solution very closely. This suggests that if equation (13) cannot be solved analytically due to the complexity of the soil water retention function used, one can try to work out $\mathrm{E}[r_1]$ by equation (A1) and replace r_1 in equation (12) with $\mathrm{E}[r_1]$ to obtain an approximate solution. For example, if the water retention curve is expressed by the *Van Genuchten* [1980] model:

$$S_{le}=\left[1+(\alpha_v\Psi_m)^{n_v}\right]^{\frac{1-n_v}{n_v}}, \tag{A3}$$

where α_v (m^{-1}) and n_v (−) are fitting parameters, then $\mathrm{E}[r_1]$ can be calculated by:

$$\begin{aligned}\mathrm{E}[r_1]=\int_0^{r_m} r_1 f(r_1)dr_1=\int_0^{r_m}\frac{r_1}{S_{le}}\frac{\partial S_{le}}{\partial r_1}dr_1=\zeta\alpha_v\left\{\left[1+\left(\frac{\alpha_v\zeta}{r_m}\right)^{n_v}\right]^{\frac{n_v-1}{n_v}}-\left(\frac{\alpha_v\zeta}{r_m}\right)^{n_v-1}\right\}\\ =\zeta\alpha_v\left\{\left[1+(\alpha_v\Psi_m)^{n_v}\right]^{\frac{n_v-1}{n_v}}-(\alpha_v\Psi_m)^{n_v-1}\right\}.\end{aligned} \tag{A4}$$

Combining equation (3), (12) (20), (21), and (A4), one gets the approximate solution of the surface resistance based on the soil water retention curve proposed by *Van Genuchten* [1980].

Notation

Ψ_0 matric potential that corresponds to zero liquid water saturation (−50,000 m).
Ψ_m matric potential (m).
Ψ_b air entry potential (m).
Ψ_p matric potential in the near-surface soil layer corresponding to the initial liquid water saturation at early stage IV (m).
α_v fitting parameter for the van Genuchten soil water retention curve.
β parameter to establish a linear relation between S_l below residual and $\ln(-\Psi_m)$ $(=[\ln(-\Psi_0)-\ln(-\Psi_m)]/[\ln(-\Psi_0)]$, –).
δ thickness of the external diffusive layer (m).
ζ constant under the assumption that the contact angle is zero ($=-2\sigma/\rho_l g$ or -1.469×10^{-5} m^2).

η	enhancement factor of vapor (−).
θ	contact angle (rad).
θ_l	volumetric liquid water content (−).
θ_{le}	effective liquid water content (−).
θ_{leTSL}	effective liquid water content in the TSL (−).
θ_{lr}	residual liquid water content (−).
θ_p	porosity (−).
λ	parameter related to the pore size distribution (−).
ρ_l	density of liquid water (1000 kg m^{-3}).
ρ_v	actual density of vapor (kg m^{-3}).
ρ_{v1}	actual density of vapor at the vaporization plane (kg m^{-3}).
ρ_{v2}	actual density of vapor at the sphere that cover the surface of the building block (kg m^{-3}).
ρ_{vRef}	actual density of vapor at the reference point (kg m^{-3}).
ρ_{vb}	actual density of vapor at the upper boundary of the EDL (kg m^{-3}).
ρ_v^*	saturated density of vapor (kg m^{-3}).
σ	surface tension (0.072 kg s^{-2}).
τ	tortuosity of vapor in soils (−).
τ_0	tortuosity of liquid water in soils when the liquid water saturation is zero (0.66–).

Roman Symbols

D_v	diffusivity of vapor (m^2 s^{-1}).
$F()$	cumulative density of water-saturated pores (−).
$G(r_m, r_b, \lambda)$	correction function (−).
K_{vr}	relative conductance of vapor through the soil-air interface (−).
K_{vr}^c	relative conductance of vapor through the soil-air interface contributed to by the vaporization of the capillary water in the topmost soil layer (−).
K_{vr}^v	relative conductance of vapor through the soil-air interface contributed to by vapor generated from the vaporization plane beneath the dry soil layer (−).
M_w	molecular weight of water (0.018 kg mol^{-1}).
Q_v^c	volumetric vapor flux through the soil-air interface contributed to by the vaporization of the capillary water in the topmost soil layer (m^3 s^{-1}).
R	ideal gas constant (8.314 J mol^{-1} K^{-1}).
S_l	volumetric liquid water saturation (−).
S_{le}	effective liquid water saturation (−).
S_{lr}	residual liquid water saturation (−).
T	temperature (K).
d	average soil particle size (m).
$f()$	probability density function (PDF) of the water-saturated pores.
g	magnitude of gravitational acceleration (9.81 m s^{-2}).
h_r	relative humidity (−).
k_{vr}^c	relative vapor conductance from one building block with the radius of water-saturated pore as r_1 contributed to by the vaporization of the capillary water (−).
l	thickness of the dry soil layer (m).
l_0	thickness of the near-surface soil layer (m).
n	exponent parameter in the correction function (−).
n_v	fitting parameter in the van Genuchten water retention curve (−).
q_v	vertical vapor flux, positive upward (m s^{-1}).
r	radius of pore in soil (m).
r_{avg}	average pore radius (m).
r_1	radius of water-saturated pores (m).
r_2	radius of cylinder building block (m).
r_a	aerodynamic resistance (s m^{-1}).
r_b	radius corresponding to Ψ_b according to the Young-Laplace equation (m).

r_s surface resistance (s m^{-1}).
r_m radius that corresponds to Ψ_m according to the Young-Laplace equation (m).
z vertical coordinate, positive upward (m).

Acknowledgments
This work was supported by the National Basic Research Program of China (973 Program-2012CB417005, 51279056 and 51479069) and National Centre for Groundwater Research and Training (NCGRT). The authors express their gratitude to the Editors and the anonymous reviewers for their valuable suggestions. The data related to this research are available to all interested researchers upon request.

References

Bear, J., and A. H.-D. Cheng (2010), *Modeling Groundwater Flow and Contaminant Transport*, Springer, N. Y.
Bird, R. B., W. E. Stewart, and E. N. Lightfoot (2002), *Transport Phenomena*, 2nd ed., John Wiley, Hoboken, N. J.
Brooks, R., and A. Corey (1964), Hydraulic properties of porous media, *Hydrol. Pap. 3*, Colo. State Univ., Fort Collins.
Brutsaert, W. (1982), *Evaporation Into the Atmosphere: Theory, History, and Applications*, D. Reidel Publ., Dordrecht, Netherlands.
Burdine, N. T., L. S. Gournay, and P. P. Reichertz (1950), Pore size distribution of petroleum reservoir rocks, *Trans. Am. Inst. Min. Metall. Pet. Eng.*, *189*, 195–204.
Camillo, P. J., and R. J. Gurney (1986), A resistance parameter for bare-soil evaporation models, *Soil Sci.*, *141*(2), 95–105, doi:10.1097/00010694-198602000-00001.
Childs, E. C., and N. Collis-George (1950), The permeability of porous materials, *Proc. R. Soc. London, Ser. A*, *201*(1066), 392–405, doi:10.1098/rspa.1950.0068.
Cooke, J. (1967), Some theoretical considerations in stomatal diffusion: A field theory approach, *Acta Biotheor.*, *17*, 95–124.
Daamen, C., and L. Simmonds (1996), Measurement of evaporation from bare soil and its estimation using surface resistance, *Water Resour. Res.*, *32*(5), 1393–1402.
Fayer, M. J., and C. S. Simmons (1995), Modified soil water retention functions for all matric suctions, *Water Resour. Res.*, *31*(5), 1233–1238.
Fujimaki, H., T. Shimano, M. Inoue, and K. Nakane (2006), Effect of a salt crust on evaporation from a bare saline soil, *Vadose Zone J.*, *5*(1994), 1246–1256, doi:10.2136/vzj2005.0144.
Gates, J. I., and W. T. Lietz (1950), *Relative Permeabilities of California Cores by the Capillary-Pressure Method*, pp. 285–298, Am. Pet. Inst., N. Y.
Haghighi, E., E. Shahraeeni, P. Lehmann, and D. Or (2013), Evaporation rates across a convective air boundary layer are dominated by diffusion, *Water Resour. Res.*, *49*, 1602–1610, doi:10.1002/wrcr.20166.
Idso, S., R. Reginato, R. Jackon, B. Kimball, and F. Nakayama (1974), The three stages of drying of a field soil, *Soil Sci. Soc. Am. Proc.*, *38*(5), 831–837, doi:10.2136/sssaj1974.03615995003800050037x.
Kondo, J., and N. Saigusa (1990), A parameterization of evaporation from bare soil surfaces, *J. Appl. Meteorol.*, *29*(4), 386–390.
Le Bray, Y., and M. Prat (1999), Three-dimensional pore network simulation of drying in capillary porous media, *Int. J. Heat Mass Transfer*, *42*(22), 4207–4224, doi:10.1016/S0017-9310(99)00006-X.
Lehmann, P., S. Assouline, and D. Or (2008), Characteristic lengths affecting evaporative drying of porous media, *Phys. Rev. E*, *77*(5), 056309, doi:10.1103/PhysRevE.77.056309.
Millington, R., and J. Quirk (1961), Permeability of porous solids, *Trans. Faraday Soc.*, *57*, 1200–1207.
Mualem, Y. (1976), A new model for predicting the hydraulic conductivity of unsaturated pore meida, *Water Resour. Res.*, *12*(3), 513–522.
Or, D., P. Lehmann, E. Shahraeeni, and N. Shokri (2013), Advances in soil evaporation physics—A review, *Vadose Zone J.*, *12*(4), 1–45, doi:10.2136/vzj2012.0163.
Parlange, J. Y., and P. E. Waggoner (1970), Stomatal dimensions and resistance to diffusion, *Plant Physiol.*, *46*(2), 337–342.
Philip, J., and D. De Vries (1957), Moisture movement in porous materials under temperature gradients, *Trans. AGU*, *38*(2), 222–232.
Prat, M. (2007), On the influence of pore shape, contact angle and film flows on drying of capillary porous media, *Int. J. Heat Mass Transfer*, *50*(7–8), 1455–1468, doi:10.1016/j.ijheatmasstransfer.2006.09.001.
Purcell, W. R. (1949), Capillary pressures—Their measurement using mercury and the calculation of permeability therefrom, *Trans. Am. Inst. Min. Metall. Pet. Eng.*, *186*, 39–46.
Ren, J. L., Q. F. Li, M. X. Yu, and H. Y. Li (2012), Variation trends of meteorological variables and their impacts on potential evaporation in Hailar region, *Water Sci. Eng.*, *5*(2), 137–144.
Rose, D. A. A., F. B. Konukcu, and J. W. A. Gowing (2005), Effect of watertable depth on evaporation and salt accumulation from saline groundwater, *Soil Res.*, *43*(5), 565–573.
Saito, H., J. Šimůnek, and B. Mohanty (2006), Numerical analysis of coupled water, vapor, and heat transport in the vadose zone, *Vadose Zone J.*, *5*, 784–800, doi:10.2136/vzj2006.0007.
Sakaki, T., A. Limsuwat, K. M. Smits, and T. H. Illangasekare (2008), Empirical two-point α-mixing model for calibrating the ECH 2 O EC-5 soil moisture sensor in sands, *Water Resour. Res.*, *44*, W00D08, doi:10.1029/2008WR006870.
Saravanapavan, T., and G. D. Salvucci (2000), Analysis of rate-limiting processes in soil evaporation with implications for soil resistance models, *Adv. Water Resour.*, *23*(5), 493–502, doi:10.1016/s0309-1708(99)00045-7.
Schlünder, E. (1988a), On the mechanism of the constant drying rate period and its relevance to diffusion controlled catalytic gas phase reactions, *Chem. Eng. Sci.*, *43*(10), 2685–2688, doi:10.1016/0009-2509(88)80012-5.
Schlünder, E. (1988b), Uber den Mechanismus des ersten Trocknungsabschnittes und seine mogliche Bedeutung fur diffusionskontrollierte katalytische Gasphasen-Reaktionen, *Chem. Ing. Tech.*, *60*(2), 117–120.
Shahraeeni, E., P. Lehmann, and D. Or (2012), Coupling of evaporative fluxes from drying porous surfaces with air boundary layer: Characteristics of evaporation from discrete pores, *Water Resour. Res.*, *48*, W09525, doi:10.1029/2012WR011857.
Shimojima, E., A. Curtis, and J. Turner (1990), The mechanism of evaporation from sand columns with restricted and unrestricted water tables using deuterium under turbulent airflow conditions, *J. Hydrol.*, *117*, 15–54, doi:10.1016/0022-1694(90)90085-C.
Shokri, N., and D. Or (2011), What determines drying rates at the onset of diffusion controlled stage-2 evaporation from porous media?, *Water Resour. Res.*, *47*, W09513, doi:10.1029/2010WR010284.
Shokri, N., P. Lehmann, P. Vontobel, and D. Or (2008), Drying front and water content dynamics during evaporation from sand delineated by neutron radiography, *44*, W06418, doi:10.1029/2007WR006385.
Smits, K. M., A. Cihan, T. Sakaki, and T. H. Illangasekare (2011), Evaporation from soils under thermal boundary conditions: Experimental and modeling investigation to compare equilibrium- and nonequilibrium-based approaches, *Water Resour. Res.*, *47*, W05540, doi:10.1029/2010WR009533.
Smits, K. M., V. V. Ngo, A. Cihan, T. Sakaki, and T. H. Illangasekare (2012), An evaluation of models of bare soil evaporation formulated with different land surface boundary conditions and assumptions, *Water Resour. Res.*, *48*, W12526, doi:10.1029/2012WR012113.
Suzuki, M., and S. Maeda (1968), On the mechanism of drying of granular beds, *J. Chem. Eng. Jpn.*, *1*(6), 26–31, doi:10.1252/jcej.1.26.
Van Brakel, J. (1980), Mass transfer in convective drying, in *Advances in Drying*, pp. 217–267, Hemisphere, Washington, D. C.

Van de Griend, A., and M. Owe (1994), Bare soil surface resistance to evaporation by vapor diffusion under semiarid conditions, *Water Resour. Res.*, *30*(2), 181–188.

Van Genuchten, M. T. (1980), A closed-form equation for predicting the hydraulic conductivity of unsaturated soils, *Soil Sci. Soc. Am. J.*, *8*, 892–898.

Wilson, G. W., D. G. Fredlund, and S. L. Barbour (1994), Coupled soil-atmosphere modelling for soil evaporation, *Can. Geotech. J.*, *31*(2), 151–161.

Yiotis, A. G., A. G. Boudouvis, A. K. Stubos, I. N. Tsimpanogiannis, and Y. C. Yortsos (2004), Effect of liquid films on the drying of porous media, *AIChE J.*, *50*(11), 2721–2737, doi:10.1002/aic.10265.

Yiotis, A. G., I. N. Tsimpanogiannis, A. K. Stubos, and Y. C. Yortsos (2007), Coupling between external and internal mass transfer during drying of a porous medium, *Water Resour. Res.*, *43*, W06403, doi:10.1029/2006WR005558.